Out-of-Core
Helium Bubbling
in the
Molten Salt
Fast Reactor

Master Thesis Applied Physics

August 2020

L. Rozing
4280229

TU Delft

Out-of-Core Helium Bubbling in the Molten Salt Fast Reactor

by

L. Rozing

to obtain the degree of Master of Science
at the Delft University of Technology,
to be defended publicly on Friday August 28, 2020 at 1:00 PM.

Student number:	4280229	
Project duration:	September 2, 2019 – August 28, 2020	
Thesis committee:	Prof. dr. ir. J.L. Kloosterman,	TU Delft, supervisor
	Dr. ir. M. Rohde,	TU Delft, supervisor
	Dr. L. Portela,	TU Delft

TUDelft

Preface

Since the 1950s, a lot has been researched about nuclear reactors, their advantages, their disadvantages, and of course their relation to nuclear weapons. In the 50s and 60s, significant steps were made at Oak Ridge National Laboratories towards an innovative reactor, utilising Thorium and liquid fuel. This technology was then abandoned for decades, but in more recent times is being rediscovered.

A lot has not yet been fully worked out: this poses a nice opportunity for an eager student to try and make a contribution to what he thinks is a great innovation that should be pursued - the Molten Salt Fast Reactor (MSFR). This thesis focuses on the use of Helium Bubbling to remove small metallic particles from the liquid nuclear reactor fuel, and explores the possibility of doing this in an external facility, rather than in the reactor core, as is currently the considered in MSFR designs.

Originally, this was meant to be an experimental project. However, due to the 2020 Corona crisis, many experiments could eventually not be carried out and the subject had to be changed from experimental to numerical. For this reason, the emphasis throughout this thesis is mostly on what was going to be considered in the experiments, and less on what could be explored using numerical methods. Also, a significant portion of the results section is missing due to this, and work that was done in preparation is included in either the Methods or the Recommendations section.

As irritating as I found it that after months of preparation, I couldn't carry out the experiments: they now are a set of nicely worked out ideas, ready for students or researchers willing to give them a second shot.

L. Rozing
Delft, July 2020

Word of Thanks

I would like to thank, first and foremost, my supervisors Martin Rohde and Jan Leen Kloosterman, for their daily supervision, advise and help during the course of this thesis, and Luis Portela for being a committee member reviewing my work. I would also like to thank Anna Smith and Thomas Dumaire for their help and advise in and outside of the progress meetings, and Dick de Haas and John Vlieland for their help with the experimental setups.

Lastly, I would like to thank Bouke Kaaks for his much appreciated help with OpenFOAM, and my friends at 'Vreetclub de Kernreactor' for bringing some structure into my time at the reactor with the cake-breaks every Thursday at 3:00 PM and for making sure I get enough physical exercise through intense table-tennis matches.

Summary

In the Molten Salt Reactor Experiments carried out in Oak Ridge National Lab in the 1960s, it was found that the Helium Bubbles introduced into the salt for the removal of gaseous fission products, also carried with them small (sub-micron) metallic particles, most notably the fission product Molybdenum. Since these particles would normally pose the risk of plating out on the insides of the reactor, this flotation effect provides an opportunity to remove them from the fuel salt. In current MSFR designs, the Helium Bubbling is taken to be carried out in the reactor core. However, as is the topic of this Thesis, moving the bubbling to an external facility might have significant advantages.

In this Thesis, a design is proposed for an external Helium Bubbling facility using counter-current bubbling. The flow fields and void fractions in this facility are evaluated using OpenFOAM, to which then the Yoon-Luttrell model for collision efficiency is applied. Two approaches are used: firstly, salt streamlines are followed through the facility and the probability that a sub-micron particle has been taken away along that trajectory is evaluated, and secondly the entire facility is considered by taking the relative velocity of a particle with respect to a bubble at every point in combination with the gas void fraction. The first approach yielded efficiencies in the order of 10^{-3} % for sub-micron particles, the second approach gave efficiencies of roughly an order of magnitude higher. These efficiencies are highly dependent on the particle size, and are expected to be much higher for larger particles.

A second part of the thesis consisted of experiments on the flotation models using LIF- measuring techniques and fluorescent nanoparticles, however due to the Corona outbreak these experiments could eventually not be carried out and remain a research proposal for future work.

Contents

List of Symbols, Acronyms and Abbreviations

Latin symbol	Meaning	SI-Unit
a	Relative surface area	m^{-1} (m^2/m^3)
A	Frontal (cross-sectional) area	m^2
C_D	Drag coefficient	-
d_{32}	Sauter diameter	m
d_b	Bubble diameter	m
d_p	Particle diameter	m
d_s	Sparger diameter	m
F_{lg}	Mass flux from liquid to gas phase	$kg\,m^{-3}s^{-1}$
Fr	Froude number	-
H	Henry solubility coefficient	-
J_G	Superficial gas velocity	m/s
k_g	Mass transfer coefficient	m/s
L_a	Airation length	m
p	Pressure	Pa
P_a	Attachment probability	-
P_c	Collision probability	-
P_d	Detachment probability	-
Re	Reynolds number	-
r_g	Volumetric gas flow rate	m^3/s
Stk	Stokes number	-
t_i	Induction time	s
t_s	Sliding time	s
u_b	Bubble velocity	m/s
u_p	Particle velocity	m/s
u_r	Relative velocity	m/s
V_b	Bubble volume	m^3
We	Weber number	-

Greek symbol	Meaning	SI-Unit
α	Phase fraction, void fraction	-
ε_g	Gas holdup	-
μ_l	Liquid (dynamic) viscosity	Pa·s
ν_l	Liquid kinematic viscosity	m^2/s
ρ_l	Liquid density	kg/m^3
ρ_p	Particle density	kg/m^3
ϕ_a	Adhesion angle	rad
ϕ_c	Collision angle	rad
$\phi_{\max}$	Maximum possible collision angle	rad

Acronym or Abbreviation	Meaning
CFD	Computational Fluid Dynamics
ED	Equivalent diameter
Gen-IV	Generation IV (type reactors)
GSE	Generalised Sutherland Equation
LCOE	Levelized Cost Of Energy
LFTR	Liquid Fuel Thorium Reactor
LIF	Laser Induced Fluorescence
LWR	Light Water Reactor
MSFR	Molten Salt Fast Reactor
MSRE	Molten Salt Reactor Experiment
ORNL	Oak Ridge National Laboratories
PWR	Pressurised Water Reactor
SAMOFAR	Safety Assessment of the MOlten saltFAst Reactor
SAMOSAFER	Severe Accident MOdeling and Safety Assessment for Fluid-fuel Energy Reactors
sccm	Standard Cubic Centimetre per Minute
SD	Sauter Diameter
TPC	Three Point Contact
TRU	TRans Uranic element
VD	Volume Diameter

<div align="right">

1

</div>

Introduction

1.1. Energy demand and nuclear reactors

The statement that world-wide energy demands are ever increasing [1] will not come as a surprise, and in fact is one of the main challenges of this age. As environmental awareness rises, the increasing energy demand poses serious problems with regard to, among other issues, the emission of greenhouse gases through the burning of fossil fuels. Even though progress is being made in the development of emission-free energy sources, the total share of energy generated by fossil fuels is only increasing and went from 63.7% of the total electricity production in 1990 to 67% in 2014 [1].
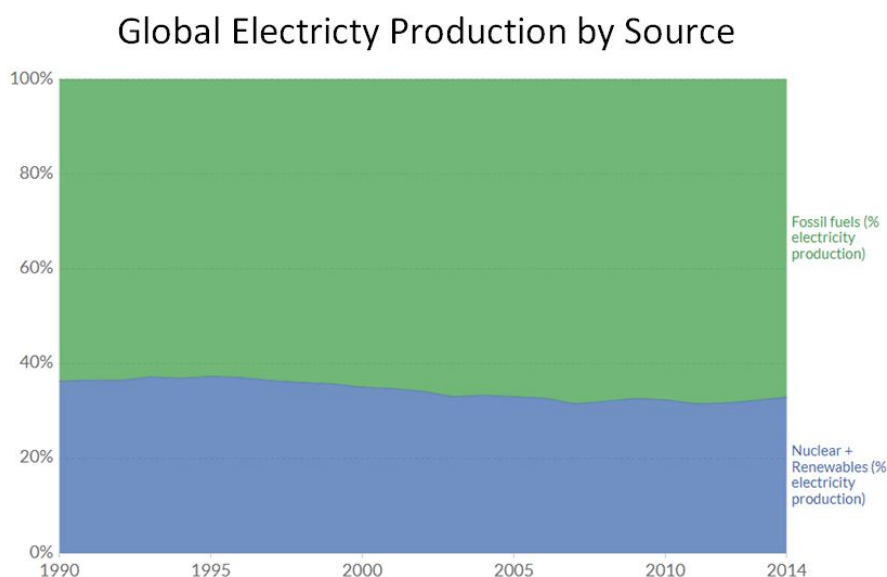
Figure 1.1: Global electricity production, measured as the percentage contribution from fossil fuels (coal, oil and gas) and low-carbon sources (nuclear, hydropower, biomass, wind, solar, geothermal and marine power) [1].

What doesn't help, is the fact that the traditional renewable energy sources (solar, hydro, wind, geothermal) have numerous downsides that make fossil fuels the 'easy way out'. Traditional renewable energy sources for example have the problem of intermittency, as the sun doesn't always shine, droughts occur, and the wind doesn't always blow. This causes the need for large scale energy storage capabilities, and/or alterations to the electricity grid to make it compatible with high peak loads. Fossil fuel sources don't have this problem, as they can be turned on and of, or up and down, at any given time. Another downside of traditional renewable energy sources is the issue of geographical limitations. A large area is needed for a solar energy plant or a wind-turbine park, and hydro-power and geothermal plants also can't just be placed anywhere.

Of course, the perks of renewable energy sources far outweigh their downsides, but they do hinder rapid development. Another source of emission-free energy, that is often not included in the list of 'green/renewable energy sources', is Nuclear Energy. Electricity from Nuclear Power Plants is generated through the fission of fissile materials, such as Uranium, and does not involve the burning of materials of any kind. Because of this, Nuclear Energy is an emission-free electricity source that does not contribute to climate change or air pollution. Also, just like fossil-fuel powered energy plants, Nuclear power plants can be operated at a range of power levels to accommodate the energy requirements at any given time. This makes it an extremely suitable option for emission-free energy production, one that doesn't have nearly as much practical downsides as traditional renewable energy sources. However, after a sharp increase in Nuclear Energy production between the 1970s and 1990s in which global Nuclear energy production went from 2% of the total to 18%, it hasn't grown much since, and in fact nowadays is back down to about 10% of the global energy production [1].
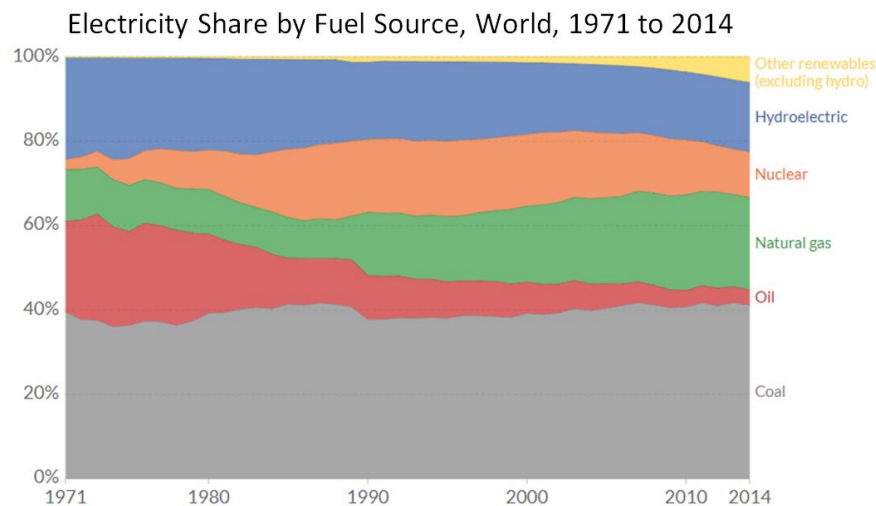
Figure 1.2: Electricity production (measured as the percentage of total electricity production) by source (coal, oil, gas, nuclear, hydroelectric power and other renewables). Other renewables in this definition includes biomass, wind, solar, geothermal, and marine power [1].

1.1.1. Challenges of Nuclear Energy

Naturally, Nuclear Power has its challenges as well. The average cost of one kWh of generated electricity over the lifetime (LCOE: Levelized Cost Of Energy, total monetary expenses of construction and operation during the total lifetime divided by total electricity generated during this lifetime) of a Nuclear Reactor is relatively high compared to alternatives, mostly due to high construction costs [2]. However, the use of the LCOE is not unanimously accepted as a suitable means of cost-efficiency estimations [3][4][5][6]. Another, perhaps the most important, downside of Nuclear Energy is the nuclear waste it produces. On average, the waste produced by a nuclear reactor is for 90% made up of so-called 'low level waste'; lightly contaminated items such as tools and work clothing. Low level waste accounts for about 1% of the total radioactivity of the produced nuclear waste [7]. On the other end, there is the so called 'high level waste': highly radioactive nuclear waste, containing spent fuel. It accounts for 3% of the total waste volume but 95% of the radioactivity. Usually, this nuclear waste is stored deep underground in reinforced containers, so minimise the possibility of radiation or radioactive materials ending up in the environment. This type of waste contains short-lived fission products, that decay relatively quickly, and long-lived actinides, that have elevated levels of radiotoxicity for as long as thousands of years in the case of Uranium actinides from Pressurised Water Reactors [8] as shown in figure 1.5. The fact that nuclear waste remains radiotoxic for such long periods of time causes Nuclear Energy to be a controversial topic in politics, hindering its development [9]. Of course, accidents like those in Chernobyl and more recently Fukushima, as well as the public's association of anything 'nuclear' to atomic weapons, don't particularly help Nuclear Energy's reputation either.

1.2. The Thorium Fuel Cycle

1.2.1. Nuclear Fuel

Conventional Pressurised Water Reactors (PWRs) use UO_2 pallets with enriched Uranium as fuel. Natural Uranium contains about 99.3% U-238, which is in itself not fissile, and 0.7% U-235, which is fissile. Through enrichment, the amount of U-235 is increased to about 4.5% in Light Water Reactors. In Research Reactors, the enrichment grade is usually higher, around 20% [10]. Once struck by a neutron with the right amount of energy, a U-235 core can undergo fission: it splits in two, releasing not only two large fragments (the fission products), but also new neutrons and a lot of energy. The fission products created are radioactive, and by decay release delayed neutrons that are essential for the operation of the reactor.
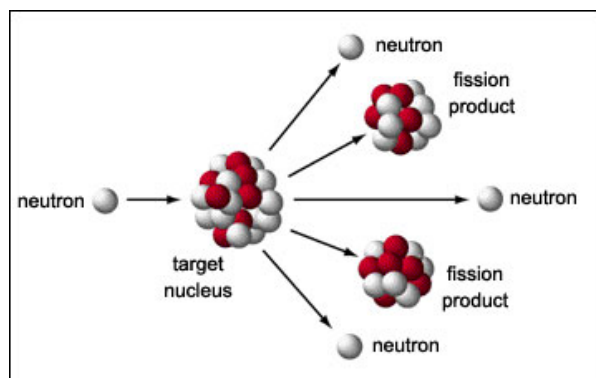

Figure 1.3: The principle of nuclear fission [11].

A problem that arises in a conventional PWR, is that because of the use of solid fuel pellets, many fission and decay products remain in the pallets and decrease the 'usefulness' of the fuel by absorbing the neutrons originally meant to cause fission of U-235. After about a year, the fissile Uranium concentration will have dropped to roughly 1% and the fuel element will have to be replaced by a fresh one, even though roughly 96% of the original amount of Uranium is still in there [12]. This causes the spent fuel waste to be full of Uranium and long-lived actinides, created by neutron captures which did not lead to fission. These actinides are the main contributor to the long-term radiotoxicity of nuclear waste.

1.2.2. Breeding and Nuclear Waste

However, U-235 is not the only isotope suitable for the generation of power. Just like U-235, U-233 is a fissile isotope and capable of sustaining a fission chain reaction. U-233 does not naturally occur, but can be 'bred' from Thorium-232 by making the latter absorb a neutron, after which through decay to Proactinium it finally decays to U-233. Thorium-232 is called a 'fertile' isotope, U-233 is fissile. Thorium is very abundant in the Earth's crust: about four times as abundant as Uranium [13]. Since there is no U-238 concerned with the Thorium fuel cycle, but instead mostly lighter isotopes, the actinide spectrum created in this cycle is vastly different from that of the fission process of enriched natural Uranium. In fact, the actinides created in the Thorium fuel cycle have a radiotoxicity of up to a factor 10^4 less than the actinides of the Uranium-Plutonium fuel cycle [8].

$$\overset{neutron}{n} + {}^{232}_{90}\mathrm{Th} \longrightarrow {}^{233}_{90}\mathrm{Th} \overset{\beta^-}{\longrightarrow} {}^{233}_{91}\mathrm{Pa} \overset{\beta^-}{\longrightarrow} \overset{fuel}{{}^{233}_{92}\mathrm{U}}$$
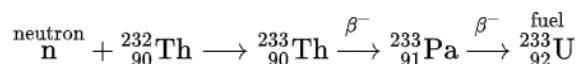
Figure 1.4: Schematic of the production of U-233 from Th-232.

The radiotoxicity of the nuclear waste from the Thorium fuel cycle will decay to Uranium-ore radiotoxicity levels in as little as 300 years (if one assumes its inventory being continuously used in operation), whereas for conventional solid-fuel reactors utilising the Uranium-Plutonium cycle, this takes in the order of 10^5 years.
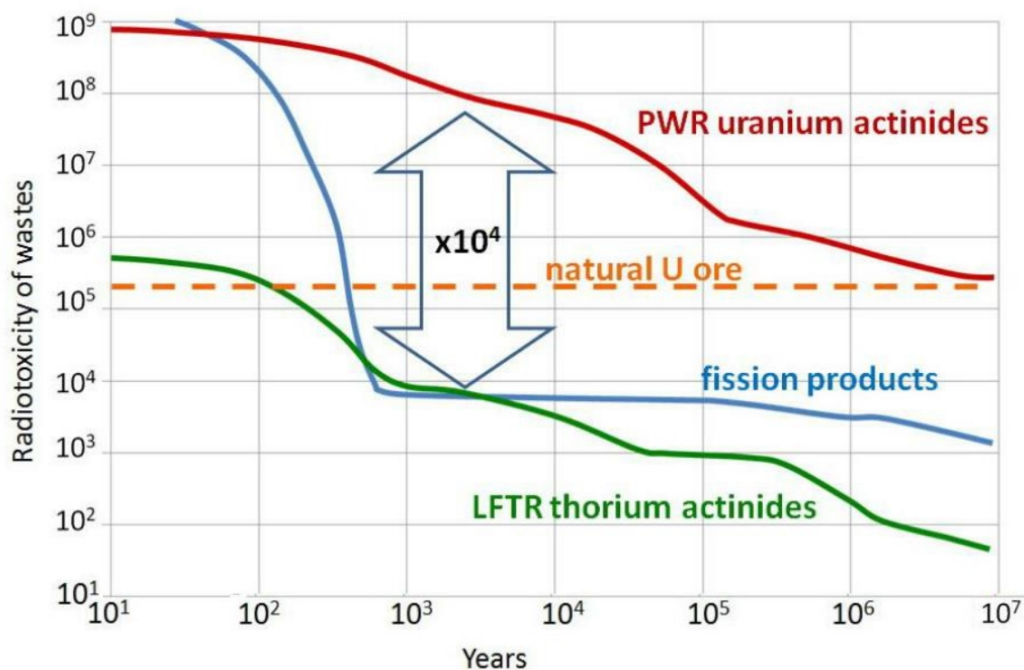
Figure 1.5: Graph of the radiotoxicity levels of nuclear waste (containing both Fission Products and Actinides) comparing PWRs to Liquid Fueled Thorium Reactors [8].

1.2.3. Nonproliferation

Another advantage of using the Thorium cycle, especially in liquid fuel reactor, is that it is much less suitable for the production of nuclear weapons. Not only is Plutonium absent from Thorium reactors, but when U-233 is created from Thorium-232, U-232 is produced as well. U-232 is a radioactive isotope with a half life of about 73.6 years, which is very difficult to separate from U-233 and decays to hard gamma emitters [13]. These hard gammas are damaging to electronics and pose a radiological hazard, limiting the usefulness of byproducts from the Thorium cycle in weaponry.

1.3. GenIV and SAMOSAFER

Not only the composition of the fuel can be varied, for the form of it there are multiple options too. As mentioned before, traditional nuclear reactors use solid Uranium-oxide fuel pallets. An alternative to this, would be Liquid Nuclear Fuel. By incorporating fissile nuclides into a salt composition, in molten form this can be used in specially designed nuclear reactors that use the flowing, hot, molten salt for electricity production. This has a number of advantages: the fission products, mentioned earlier as the cause for solid fuel elements to need replacement, can be removed from the salt which in turn can be re-fuelled with fresh fuel salt. Since this liquid fuel is continuously flowing, a liquid fuel nuclear reactor allows for on-line reprocessing. This reactor type, fittingly called the Molten Salt Reactor, is one of the Generation-IV (GenIV) reactor concepts. GenIV is the latest generation of nuclear reactors, not yet in operation but currently intensively being researched and developed to possibly be deployed in the middle-long term (2030-2050) [14].

SAMOSAFER (Severe Accident MOdeling and Safety Assessment for Fluid-fuel Energy Reactors) is a joint research project by a number of universities and research institutes lead by the TU Delft, that analyses the operation and safety features of the Molten Salt (Fast) Reactor. It is the successor of the SAMOFAR (Safety Assessment of the MOlten saltFAst Reactor) project that was finished in 2019.
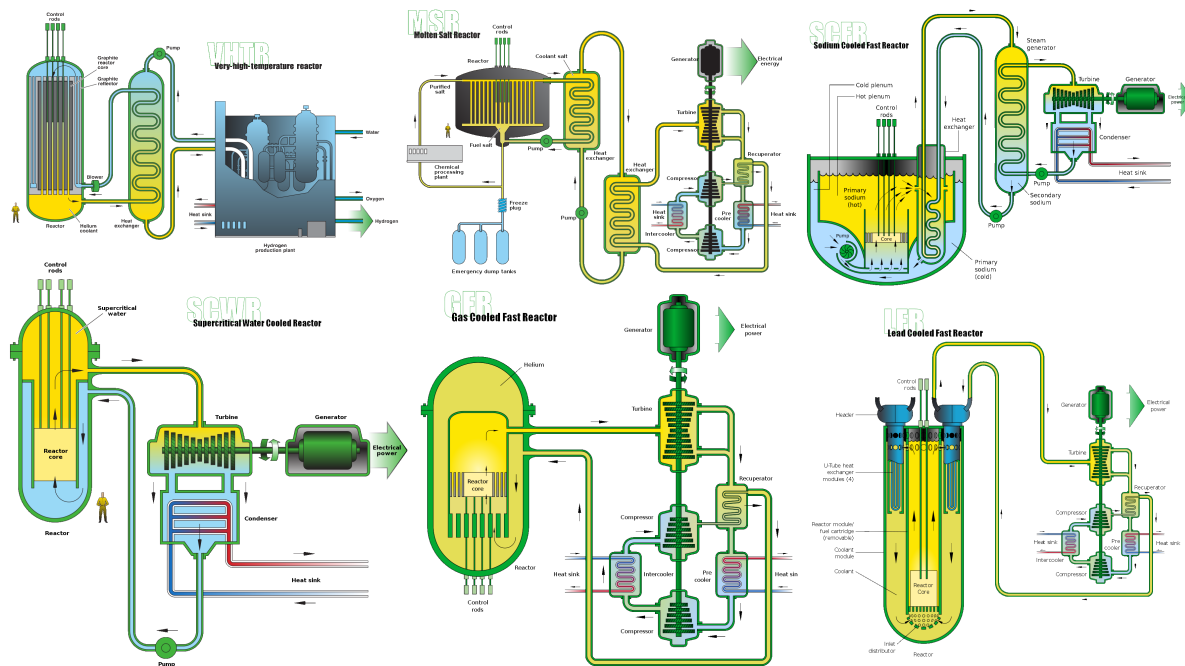
Figure 1.6: The six Generation-IV reactors. Clockwise from top left: the Very High Temperature Reactor, the Molten Salt Reactor, the Sodium Cooled Fast Reactor, the Supercritical Water Cooled Reactor, the Gas Cooled Fast Reactor and the Lead Cooled Fast Reactor [15].

1.4. The MSFR

The Molten Salt Fast Reactor (MSFR) is a type of Gen-IV Molten Salt Reactor that utilises unmoderated neutrons, i.e. in the fast spectrum. As opposed to moderated Molten Salt Reactors, which have graphite channels in the core through which the fuel flows, the MSFR consists of a core which more or less is a basin filled with the molten fuel salt. At the top and the bottom of this basin, the salt respectively leaves and enters through pipelines which are connected to a heat exchanger that cools down the salt and uses the heat to power turbines that generate electricity. Since the salt is both the fuel (that heats up as a result of fission) and the coolant, no additional loop is required between the salt and the heat exchanger (which, like conventional reactors, uses water). A seperate loop is present between the first heat exchanger and the energy conversion system. The slightly cooler salt, after passing the heat exchanger, enters the basin again and repeats the cycle.

The fuel that is used in the MSFR starts out as a Thorium-Fluoride salt, which initially resides at the outer edges of the reactor core as a sort of 'blanket' against the wall. As a result of the fission processes that are going on in Uranium-containing salt (or 'start-up' fuel) in the reactor core, unmoderated neutrons will be released there that will reach the Thorium salt residing outside of the core. After absorbing these neutrons, the Thorium will eventually decay to the fissile Uranium-233. Now being fissile rather than fertile, the salt (now containing Uranium-233) is suitable for use in the reactor core. The salt is lead from the blanket into the core, where it will undergo fission, releasing both heat and neutrons that will convert more Thorium to Uranium within this previously described 'blanket'. In this continuously repeating process, the reactor generates its own fissile material. Reactors that have this property are called 'Breeder Reactors'.

This type of reactor has a number of advantages over current Light Water Reactors. For one, it operates at atmospherical pressure, so there is no risk of anything blowing up. Another advantage of this reactor, is that it has an innovative 'freeze plug' at the bottom of the core. Underneath the reactor is a secure (empty) basin, meant for the salt to flow to, might anything go seriously wrong. During normal operation, the salt is prevented from draining into this basin by a plug of frozen salt, which is continuously being electrically cooled. In case of a loss of power, the cooling will stop and the plug will melt, causing the fuel to safely drain into the basin underneath where it can do no harm.

As stated earlier, the use of liquid fuel allows for both on-line and off-line reprocessing of fuel. The latter

is done in a re-processing plant, where a portion of the salt flows through to be chemically cleaned of fission products and re-filled with fuel. On-line extraction of fission products happens through Helium-Bubbling: as Helium bubbles are lead through the salt, they take with them the gaseous Xenon (and other dissolved gases) and through flotation also a portion of the solid, metallic fission products that are present in the salt. The latter part will be the main topic of this thesis.
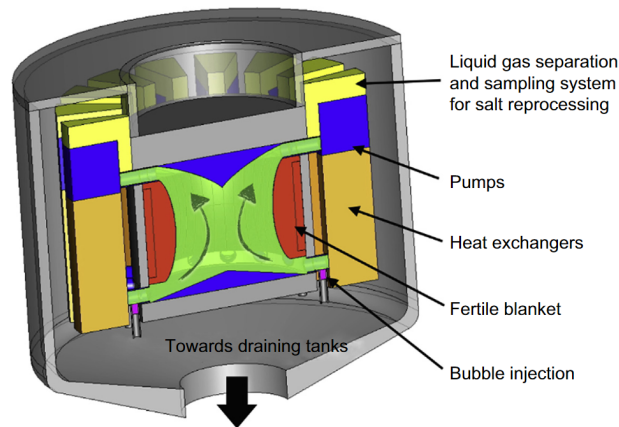
Figure 1.7: Schematic representation of the Molten Salt Fast Reactor. In current designs, Helium Bubbling is (exclusively) done inside the core [16].

1.5. Oak Ridge National Laboratory

Molten Salt Reactor technologies or the use of Thorium are far from new. In fact, in the 50s and 60s already these technologies were researched. The Oak Ridge National Laboratory in Tennessee conducted research on the Molten Salt Reactor throughout the 1960s in the so called Molten-Salt Reactor Experiment, or MSRE. The reactor they built went critical in 1965 and remained in operation (although not continuously) until 1969. A lot of research was done during this time, including research on the effect of letting Helium Bubbles pass through the salt.

Figure 1.8: The core of the MSRE reactor. Unlike the Molten Salt Fast Reactor, the MSRE used a moderated reactor core, this one is made of graphite channels through which the fuel salt flowed.

Initially, this was done to remove insoluble gaseous (and neutron-poisonous) fission products from the salt, but is was found that these bubbles also take small metallic particles with them through flotation processes.
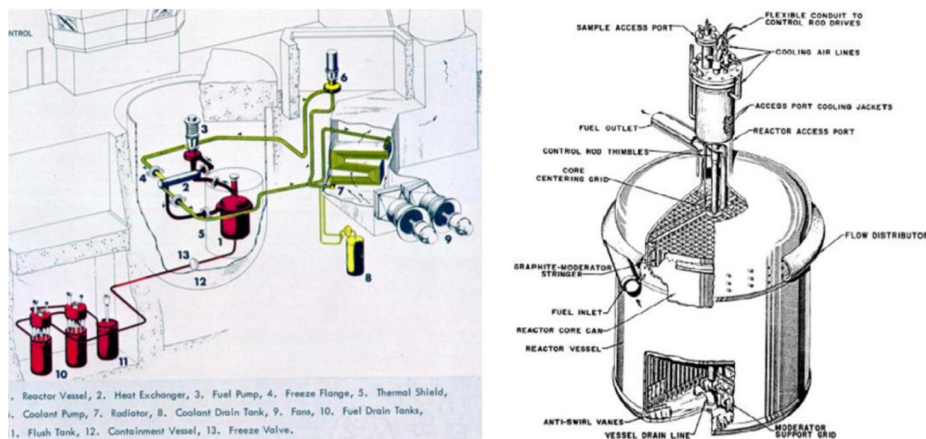
Figure 1.9: Flow diagram from the MSRE, and the reactor vessel. [17]

These particles can be both fission or corrosion products, neither of them is desirable to have in the fuel salt. This finding presents the starting point for what will be examined in this thesis: how can Helium Bubbling best be used to get rid of metallic particles in the fuel salt?

1.6. Current State of Affairs and Research Objective

The flotation mechanism is not new, and is in fact often used in mineral processing in the mining industry. In the context of the MSFR however, the effect is not yet fully described and research on it, with the aim of describing its effect as a part of MSFR operation simulations, is ongoing. NRG in Petten is working on simulations describing flotation effects in the MSFR, especially the rate with which apolar particles are removed from a volume of polar liquid as a result of flotation caused by bubbles being lead through this volume. Capelli conducted extensive research on flotation efficiencies for Molybdenum micro-particles [18], however her research focussed on larger (>1 µm) particles, and measured not directly the removal rate, but rather the amount of particles that could be recovered from a Hallimond tube after the flotation process. Since NRG is mostly interested in experimantal data on the sub-micron particle removal rate as a result of flotation for the validation of their code, this research will focus on precisely that. The effect of bubbling on the particle concentration within a volume of fluid will be experimentally determined, after which NRG can use the data to validate their code. This code can then eventually be incorporated into the MSFR simulation code, in order to obtain a more complete description of the full system.

Because of the 2020 Corona-crisis however, after many of the preparations had been made, the experiments could no longer be carried out so a different direction for this thesis was adapted. Since no system for the actual removal of the floated particles had been designed for the MSFR yet, a new idea was worked out: instead of doing the Helium Bubbling inside the reactor core, the possibility of doing it outside of the reactor core, in an external facility, was explored. This new part of the research consisted of getting to know OpenFOAM, and using it to run simulations on a new design for a Helium Bubbling Facility, to make predictions on the efficiency of the removal of the solid, metallic fission products from the fuel salt. This research could provide new insights into the possibilities with regard to the removal of fission products, and could contribute to a more complete MSFR design concept.

In this thesis, the theory behind the flotation process will be discussed, as well as the physics behind the OpenFOAM program. A design for an external Helium Bubbling Facility will be proposed, and will be computationally examined using the OpenFOAM simulations. Also, the originally planned experiments on flotation will be discussed, as will some of the results of these experiments. For the most part however, the results to this section will be absent, as most experments could not be carried out. Lastly, the conclusions of the research will be presented and discussed and an outlook for future work will be given.

$$2$$

Theory

2.1. Fission and corrosion products in the MSFR

The initial fuel in the Molten Salt Fast Reactor can be one of two possibilities, being a 77.5-20-2.5 mol% LiF-ThF$_4$-UF$_4$ salt or a 77.5-6.6-12.3-3.6 mol% LiF-ThF$_4$-UF$_4$-(TRU)F$_3$ salt, where the TRU denotes transuranic elements such as Plutonium and minor actinides, which are products of Light Water Reactors that can be 'burned up' acting as a compound of the starting fuel of the MSFR [19]. As mentioned, the MSFR is a breeder reactor that utilises the Thorium fuel cycle. Thorium-232, present in the blanket around the fuel, catches a (fast) neutron to become Thorium-233, which decays through β^--decay to Protactinium-233 which then decays through β^--decay as well, this time to the fissile Uranium-233 which is brought from the blanket into the reactor fuel. Thorium-233 has a half life of approximately 20 minutes, Protactinium-233 has a half life of just under 27 days.

2.1.1. Fission products and coalescence

Since this thesis is about a method for the extraction of fission products from the fuel salt, the fission products of Uranium-233 are examined. The composition of the fission products vary in a broad probabilistic manner, which is why there is a wide variety of fission products that are produced in the reactor fuel. In [20], an overview of the different yields of fission products from the MSRE is given. This reactor had a molten salt fuel with components similar to that of the MSFR, both utilising the Thorium fuel chain through ^{233}U. It can be seen that the most abundant fission products (in equilibrium) by mass per unit volume are Xenon (Xe), Zirconium (Zr), Cerium (Ce), Neodymium (Nd) and Molybdenum (Mo). Most of these fission products dissolve in the fuel salt. An exception however is Molybdenum, which does not dissolve in the reactor fuel but instead exists as small metallic particles in the fuel, that will eventually plate out on the colder parts of the inside of the reactor, such as the heat exchanger. Another problematic fission product is Xenon, since it has a large neutron capture cross-section and therefore hinders the fission chain reaction. Xenon is a gaseous fission product that through mass transfer can be removed by Helium Bubbling.

In this thesis, the focus is on Molybdenum. The fission products that do not dissolve in the reactor fuel (the 'noble metals') are reported to be, ordered by equilibrium mass per unit volume as found in the Oak Ridge experiments: Mo (6.006 g/ft^3), Ru (2.757 g/ft^3), Te (2.002 g/ft^3), Nb (0.376 g/ft^3) and Sb (0.114 g/ft^3), as presented in [20]. These metals are not necessarily noble in the strict sense, but were given that name because they do not react with or dissolve in the fuel salt.

From the experiments carried out at the Oak Ridge National Laboratories, it is expected that the Molybdenum particles will range in size from as small as Angströms to several microns [21]. The smaller particles are identified as individual particles, whereas the larger ones can be identified as larger clusters of individual particles. Since the fission products come into existence at an atomic level, it is very relevant to examine exactly to what size they can grow in the fuel salt. Capelli performed experiments to investigate to what size Molybdenum particles will grow in an environment similar to that of the MSFR [18]. She found that the particles are likely to grow to a size of just under half a micron.
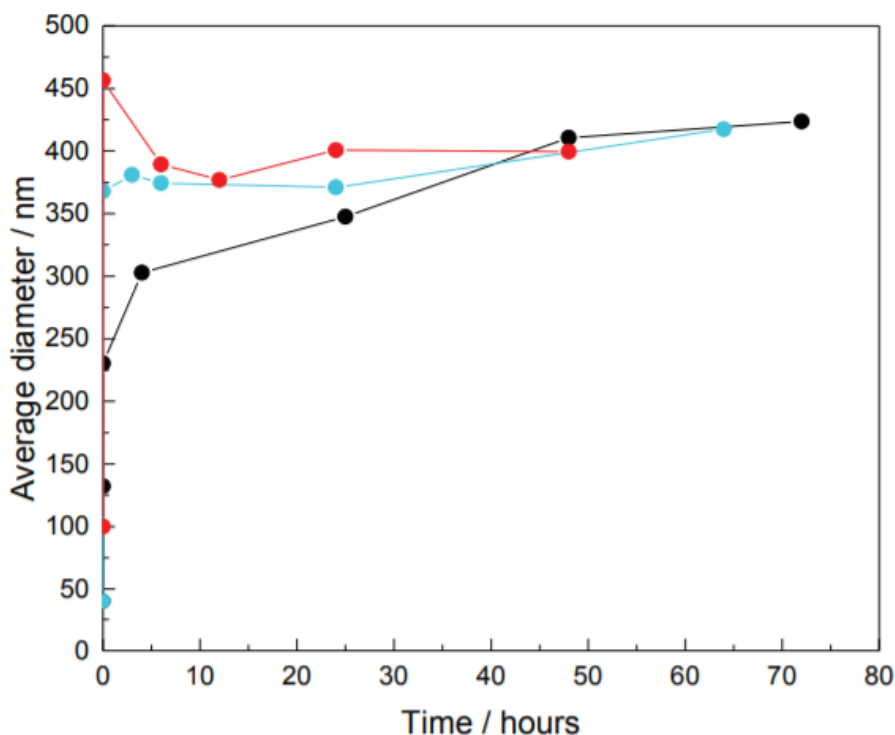
Figure 2.1: Evolution of the average particle size of molybdenum in FLiNaK at 973 K. Red points: measurements performed starting with <100 nm nanoparticles and manual mixing. Blue points: measurements performed starting with 35-45 nm nanoparticles and manual mixing. Black points: measurements performed starting with 35-45 nm nanoparticles and ball milling. [18]

2.1.2. Corrosion products

Since corrosion is very undesirable in the MSFR, or in any reactor or other system for that matter, the material of it should be chosen very carefully. The use of hot fluoride salts poses corrosion risks to materials containing Chromium, since through reduction reactions the Chromium could react with the Fluoride components in the salt [22]. This will lead to deterioration of the structural integrity of the reactor components, and introduce impurities to the fuel salt. To prevent this, the researchers at Oak Ridge have conducted experiments to single out the alloy that was best suited for use as the structural material of the reactor components that come into contact with the fuel salt. Despite containing Chromium, it was found that the alloy 'Hastelloy-N' was very suitable for use in the MSR as it has high resistance to oxidation in hot Fluoride salts, as after 9 years of operation and being exposed to air an oxide layer of at most 0.05 mm had formed, and 'voids' as a result of corrosion even after 9 years of operation were at most 0.1 mm deep [23]. Because of Hastelloy-N's good resistance to corrosion, the corrosion products are not explicitly considered in this thesis.

2.1.3. Neutron cross sections

It is important that the neutron economy is maintained at a chain-reaction supporting level inside the reactor core throughout the operation of the reactor. The fission products capturing neutrons that are meant to cause fission can hinder reactor operation, which is why their neutron capture cross sections are important. The four most abundant noble metal fission products found in dispositions are stated in [21] to be ^{99}Mo, ^{132}Te, ^{95}Nb and ^{103}Ru. Their neutron capture cross sections are given in figure 2.2.
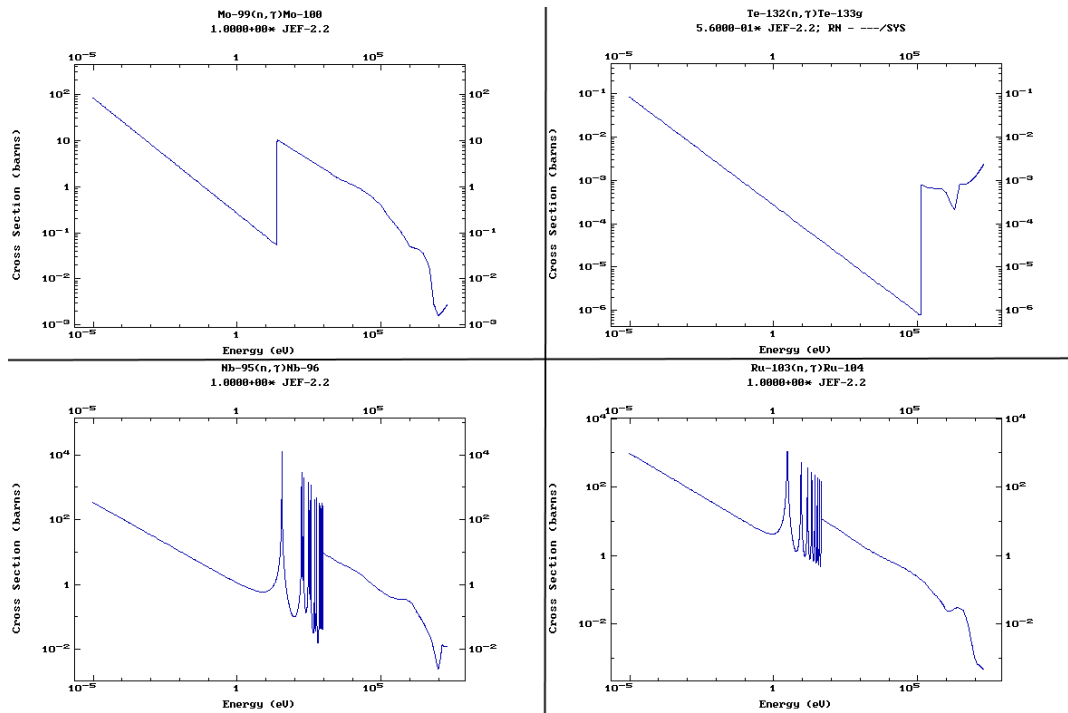
Figure 2.2: The neutron capture cross sections of (from left to right and from top to bottom) ^{99}Mo, ^{132}Te, ^{95}Nb and ^{103}Ru. [24]

2.1.4. Agglomeration of solid particles

Since the particles of interest will be of the opposite polarity compared to the fluid they are suspended in (non-polar vs polar), just as they will stick to bubbles, they will stick to themselves. As will be discussed further on, the size of the particles is of great importance to their flotability. As mentioned earlier, particles are expected to grow to a size of roughly half a micron. However, several of these particles may stick together, not so much forming a new particle in the sense that they are tightly bound, but rather in the sense that they form a loosely bound cluster of particles that gets floated all together.

This phenomenon has two important effects, one that can be considered positive and another that, at least for this thesis, is somewhat unwanted. The first effect is that the increase in particle size as a result of the agglomeration increases the flotation efficiency, as can be seen from equations that will be discussed further on. This means that in the reactor, although the particles may not grow over half a micron in size, the fact that they will tend to stick together increases the effective 'particle'-size and will thus make it easier to remove Molybdenum particles from the reactor fuel by means of flotation.

Figure 2.3: Dust sample recovered from the MSRE at Oak Ridge. Analysis showed that this sample largely consisted of fuel salt, and 2-3% of this sample to be fission products. It can be seen that the smallest particles are in de order of tenths of microns, the larger clusters in the order of microns. [25]

A downside of this effect, at least for as far as this thesis is concerned, is that it obscures data on the size of the particles that were floated in experiments. It is difficult to relate the agglomeration of particles in the experimental setup (which will be introduced later on) to 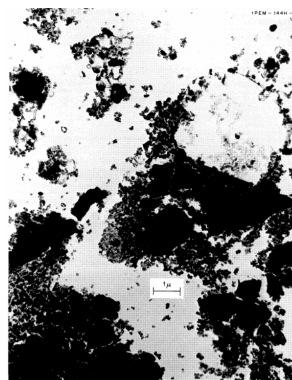the agglomeration of particles in the MSFR, as the flow of the fluid for example is expected to have great influence on the effect, since the flow dictates the particle velocities and with that, influences the local concentrations. Also, it is difficult to analyse to what extent agglomeration has occurred within the experimental setup as the particles cannot be traced individually. This makes it a challenge to make meaningful statements about the 'true' particle size in the experiments.

2.2. Helium Bubbling in Liquid Fuel Reactors

In liquid fuel reactors, unwanted fission products can (and therefore should) be removed from the fuel salt, especially from the core where fission events mainly happen. One way to achieve this removal of fission products is by letting bubbles of an inert gas, such as Helium, bubble through the fuel as was done in the MSRE. Via mass transfer, gaseous fission products that are dissolved in the fuel are taken up by the Helium bubbles as will be explained later. This way, highly neutron-poisonous gaseous fission products such as Xenon could be transported to an off-gas system where they can be removed from the fuel cycle [26].

In the MSRE, it was found that noble metal fission products (which are unwet by the fuel salt) display 'salt fleeing'-behaviour due to their non-polarity: the particles adhere to surfaces of other materials in the reactor [21]. This is problematic, as these noble metal particles will eventually end up plating out on the insides of the reactor, for instance on the heat exchanger. When this happens, proper heat transfer is impeded which is detrimental to the efficiency of the operation of the reactor.

This is why it is desirable to incorporate a system into Molten Salt Reactors that extracts the noble metal fission products from the fuel salt. In the MSRE it was found that the noble metal particles adhere to the Helium bubble surfaces due to their salt-fleeing nature [21]. Once attached to a Helium bubble, a noble metal particle is floated to the surface and thus can be extracted from the fuel salt. In the MSRE, this (side) effect was not yet incorporated into the design considerations, but when analysed and modeled properly, can be taken into account when designing the MSFR.

2.3. Physics of Bubbling

2.3.1. Bubbling methods

The reactor that was analysed in the MSRE differed from the MSFR in a number of aspects. The most fundamental aspect was that the reactor from the MSRE was moderated (uses thermal neutrons), whereas the MSFR is not moderated (uses fast neutrons). In practice, that means that in the MSRE, the fuel salt was flowing through fuel channels surrounded by graphite moderator. The fuel flow had a 10% bypass loop [27], in which the Helium bubbling was performed. The use of the bypass in the MSRE allowed for the use of a Venturi-type bubble generator, introducing bubbles into the end of the bypass, letting the bubbles flow through the reactor core and removing them again upon re-entry of the bypass. In the current design of the MSFR, no such bypass is used for bubbling which instead happens from the bottom of the reactor vessel. It should be noted, as stated previously, that the bubbling system in the MSRE did not serve exactly the same purpose as the bubbling system in the MSFR will do. In the MSRE, the bubbling was meant purely to extract gaseous fission products so the re-circulation of the bubbles through the entire reactor was more of a perk than a problem. In the MSFR however, these bubbles are also meant to transport noble metal particles that must be prevented from plating out. For this reason, the re-circulation of bubbles (with possibly particles attached to them) in the MSFR might diminish the effect of the flotation of these particles and might therefore well be undesirable.

There is a number of ways bubbles can be created. In general (when considering air bubbles in water), one can distinguish **dissolved air methods, electrolytic methods** and **dispersed air methods**. The latter of these three is most widely used, due to its relative simplicity. Basically, dispersed air methods come down to mechanically introducing bubbles into a liquid by means of for example nozzles or bubble distributors. In dissolved air methods, small bubbles are created by lowering the pressure in a liquid in which, when the pressure was higher, the air was introduced. Electrolytic methods make use of electrolysis in water, forming O_2 bubbles at one electrode and H_2 bubbles at the other.

As stated before, in the MSRE a Venturi-tube was used. The lay-out of it can be seen in figure 2.4. The Venturi-

tube is an example of a **dynamic distributor** and a dissolved air method of bubble generation. It relies on the flow of the fluid for the formation of bubbles, and utilises the turbulence in the narrow high velocity region (where the air/Helium is introduced) to form small bubbles. This design was chosen as it does not rely on auxiliary power sources and does not have moving parts, which were considered unnecessarily complex for use in a Molten-Salt system [27].
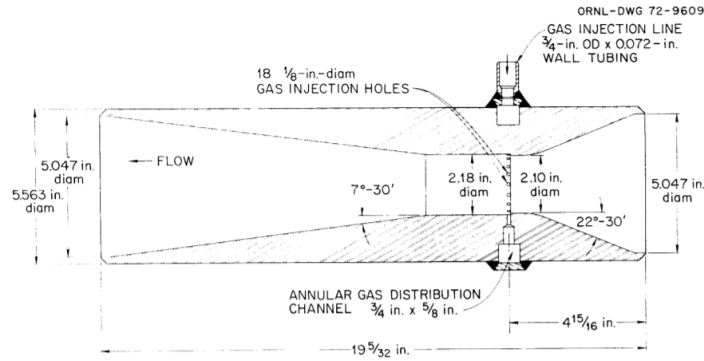

Figure 2.4: Design of the Venturi-type bubble generator for use in the MSRE. [27]

2.3.2. Bubble Properties with Porous Plate Spargers

A number of bubble properties is important for flotation purposes. These especially involve size and surface area. Since (small) bubbles are approximately circular in shape, a convenient property to define is the **volume diameter** (VD). It is defined as the diameter that is equal to the diameter of a perfect sphere with the same volume as the bubble. Another property that is convenient to define, and relates more to the surface-effects of bubbles (such as flotation), is the **Sauter diameter** (SD). The Sauter diameter is equal to the diameter of a perfect sphere that has the same volume to surface area ratio as the bubble, and is in literature sometimes denoted as d_{32}.

For a porous plate sparger, as will be used in this thesis, the (Sauter) diameter of bubbles depends on sparger, liqiud, and gas flow properties. Kazakis *et al* [28] found and experimentally validated an equation that relates these properties to the (initial) Sauter diameter of the bubbles:

$$\frac{d_{32}}{d_s} = 7.35 \left[\text{We}^{-1.7} \text{Re}^{0.1} \text{Fr}^{1.8} \left(\frac{d_p}{d_s} \right)^{1.7} \right]^{\frac{1}{5}} \tag{2.1}$$

Where d_{32} denotes the Sauter diameter, d_s the sparger diameter, d_p the pore diameter of the sparger and We, Re and Fr the Weber, Reynolds and Froude number respectively. The latter three are in this case defined as:

$$\text{We} = \frac{\rho_l d_s}{\sigma_l} J_g^2 \tag{2.2}$$

$$\text{Re} = \frac{\rho_l d_s}{\mu_l} J_g \tag{2.3}$$

$$\text{Fr} = \frac{1}{d_s g} J_g \tag{2.4}$$

In which ρ_l, σ_l, μ_l and J_g denote the density of the liquid, the surface tension of the liquid, the viscosity of the liquid and the superficial gas velocity respectively. J_g is defined as the volumetric gas flow rate divided over the cross-sectional area of the sparger. Equation 2.1 can be rewritten to:

$$d_{32} = 7.35 \left[\rho_l^{-0.32} \sigma_l^{0.34} \mu_l^{-0.02} g^{-0.36} d_s^{-0.02} d_p^{0.34} J_g^{0.06} \right] \tag{2.5}$$

2.3.3. Flow regimes

When considering bubble flow through a fluid-filled column, as will be done in this thesis, three regimes of flow-behaviour can be distinguished [29]. See figure 2.5. In the first regime, called the **homogeneous regime**

or the **bubbly flow regime**, the bubble size distribution is narrow, and no large scale circulation of fluid is present. Bubble-bubble interactions are minor and the void fraction distribution is radially uniform. In the second regime, called the **transition regime**, the bubble size distribution widens and the flow becomes unstable. The radial void fraction distribution loses its uniformity, being larger near the center and smaller in the outer regions, and large scale circulation of the fluid happens with upward flow in the center of the column and downward flow near the walls. On the far end of the flow spectrum, there is the **heterogeneous** or **churn-turbulent regime**. It is characterised by a wide bubble size distribution, where bubble sizes can differ by an order of magnitude. Bubble coalescence and break-up, which determine the bubble size, reach an equilibrium.
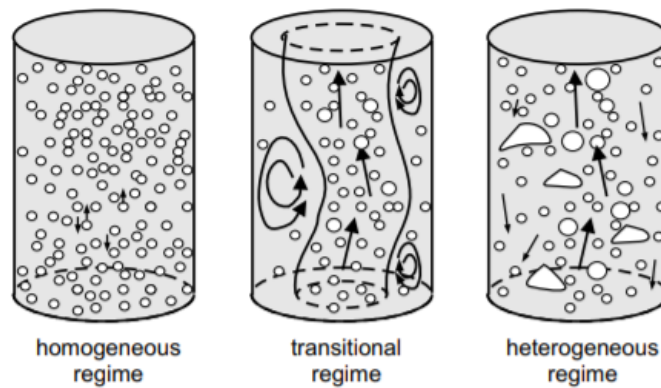
Figure 2.5: The three flow-regimes for bubble flow in a column.

When working with a narrow column, say with a diameter of no more than 15 cm, a fourth regime can be distinguished called **slug flow**. In slug flow, large bubbles are stabilised by the walls of the column.

The different regimes are the result of differing superficial gas velocities used in the bubbling column, the relation of which is shown in figure 2.6. The **gas holdup** ε_g is defined as the fraction of the liquid-gas mixture volume occupied by the bubbles.
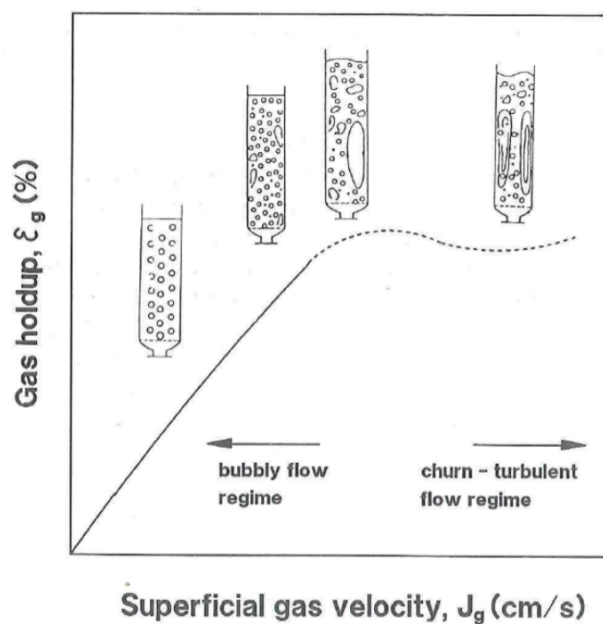
Figure 2.6: Gas holdup as function of superficial gas velocity, with different flow regimes indicated. [30]

The experiments in this research require a homogeneous flow, because this will ensure a narrow bubble size distribution and as little circulation effects as possible. Therefore, it is important that the superficial gas velocity is kept at a value that is low enough to prevent circulation of the fluid. What this means for the values will be discussed in the Methods section.

2.3.4. Bubble rise velocity

An important parameter for the evaluation of flotation processes, is the bubble rise velocity. It influences the properties of the flow around the bubble and therefore could have (and in fact does have) a significant effect on the efficiency of flotation of noble metal particles. The bubble rise velocity for small (sub-centimeter) bubbles can be calculated as follows [31]:

$$u_b = \sqrt{\frac{(\rho_l - \rho_g)g}{\frac{3}{4}\left(\frac{C_d}{d_b}\right)\rho_l}} \tag{2.6}$$

With ρ_l and ρ_g the densities of the liquid and the gas respectively, d_b the diameter of the bubble and C_d the drag coefficient, the expression for which depends on the drag model that is used. This will be discussed later on.

2.4. Interactions of Bubbles with other materials

2.4.1. Extraction of GFPs

The main concept discussed in this thesis is the interaction of the bubbles with the fission products that are to be removed from the liquid fuel. Originally, the bubbling system was designed for the removal of gaseous fission products such as Xenon. The principle that governs this, is **mass transfer**. Mass transfer is the phenomenon where a dissolved substance migrates from one phase to another, with the difference in concentration of the substance between the two phases as driving force. Krishna and Van Baten [31] derived the following relation:

$$F_{lg} = k_g a(HC_l - C_g) \tag{2.7}$$

With F_{lg} the flux of the dissolved substance from the liquid phase to the gas phase (in $\text{kg m}^{-3}\text{s}^{-1}$), k_g the mass transfer coefficient (in m/s), a the relative surface area of the bubble (in m^2/m^3) and H the dimensionless Henry solubility-coefficient, which can be expressed as the dimensionless ratio between the aqueous-phase concentration of a species and its gas-phase concentration. Since Xenon has very low solubility in the Molten Salt Reactor Fuel [32], mass transfer can be expected to be an effective means of extracting Xenon from the salt.

2.4.2. Extraction of particles by flotation

As mentioned, not only do Helium bubbles extract gaseous species from the fuel salt, solid noble-metal particles were transported by them as well. This has everything to do with the fact that the reactor fuel is a polar liquid, whereas the noble metal particles, such as Molybdenum, are non-polar. This means that the Molybdenum particles are unwet by the salt, and thus seek other surfaces to migrate to. This effect causes Molybdenum particles to adhere to the bubble surfaces, allowing them to be floated to the surface or an off-gas system.

The process of flotation hinges on three probabilities: that of particle-bubble collision P_c, particle-bubble attachment P_a and particle-bubble detachment P_d. The resulting probability of the collection of a particle through flotation P can be written as:

$$P = P_c P_a (1 - P_d) \tag{2.8}$$

Following Zhang [33], for sub-micron particles the bubble-particle aggregate is stable, causing P_d to be zero. Since this is the case assumed in this research, P_d will be omitted and the particle collection probability reduces to:
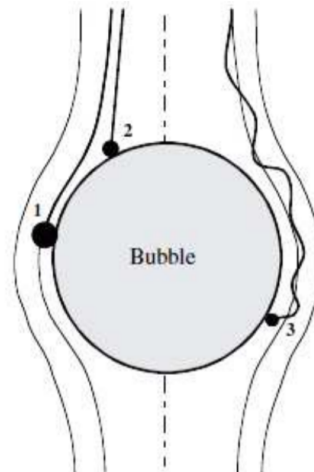
$$P = P_c P_a \tag{2.9}$$

Figure 2.7: Schematics of the (1) interception, (2) gravity and (3) Brownian transport mechanisms for particle-bubble collisions. [33]

Bubble-particle collision

For the evaluation of the particle-bubble collision probability, several things must be taken into account. First, the inertia of the particle is considered. If it is very small, it will tend to follow streamlines. This will not be the case, or at least to a lesser extent, for larger, heavier particles. An example is given in figure 2.7.
Generally speaking, the probability of particle-bubble collision can be evaluated by introducing three separate situations [34]:

1. The inertia of the particle can be neglected and only the size matters, it follows stream lines;

2. Inertial disposition is the main considered contributor to collisions;

3. Inertia should be taken into account but so should other properties.

A convenient tool to evaluate which situation should be considered, is the (dimensionless) **Stokes number (Stk)**. This number is a measure for the ratio of inertial forces of the particle over the viscous resistance of the liquid, and is defined as:

$$\text{Stk} = \frac{d_p^2 u_p \rho_p}{9\mu d_b} \tag{2.10}$$

For a small Stokes number, the first situation applies and for a large Stokes number, the second situation applies. According to Dai [34] and references therein, a 'small' Stokes number corresponds to $\text{Stk} \ll \frac{1}{12}$ and a 'large' Stokes number to $\text{Stk} \gg \frac{1}{12}$. If neither applies, the Stokes number is considered intermediate and the third situation applies.

Further following Dai [34], the three situations mentioned above can be evaluated using three different models. In the first situation, for a small Stokes number, the particle will follow the streamlines around the bubble and the process can be described by the **Sutherland model**. In the second situation, for the large Stokes number, the **Langmuir-Blodgett model** applies and in the third (intermediate) situation the **Generalised Sutherland Equation** or **GSE-model** should be used. Below is a brief description of these three models.

The Sutherland model

The Sutherland model assumes that the particle inertia can be neglected, and thus the particle follows the stream lines around the bubble. It is the size of the particle that determines whether or not the particle is intercepted. This probability can be approached as the ratio of the surface area above the bubble within which the stream lines will bring the particle into contact with the bubble (for which [34] provides an expression), divided over the area of the bubble trajectory. This way, the collision probability can be written as [34]:

$$P_{c-Su} = 3\frac{d_p}{d_b} \tag{2.11}$$

However, it should be noted that this model is only valid for high bubble Reynolds numbers. The Reynolds number for the bubbles in this thesis are in the order of 10^0 to 10^2 and thus fall into the intermediate Reynolds regime. Cheng [35] proposes an alternative for bubble Reynolds numbers in the range of 0.2 to 100:

$$P_{c-Su,C} = \left(\frac{3}{2} + \frac{4\text{Re}_b^{0.72}}{15}\right)\left(\frac{d_p}{d_b}\right)^2 \tag{2.12}$$

This equation is also mentioned in [34] as the **Yoon-Luttrell model** for intermediate Reynolds numbers, which was developed based on the same assumptions as the Sutherland model.

Another quantity that is often mentioned in literature is the **maximum possible collision angle**. This is defined as the maximum polar angle from the bubble north pole at which a particle can collide with the bubble. In the Yoon-Luttrell model, particle inertia is ignored. Kouachi *et al.* [36] (and references therein) state that when particle inertia is taken into account, the maximum possible particle collision angle can be smaller than 90°. This leads to an overestimation of the particle-bubble collision efficiency.

Another thing that should be considered, is that when taking Brownian motion into account, it is not the particle diameter that is relevant but the particle diameter plus the length of the Brownian deviations from the stream line that the particle is following. When taking this into account (but ignoring particle inertia), one can see that P_c (in the case of $\phi_{\max} = 90°$) has an underestimation in the order of the ratio of the Brownian deviation length from the stream line over the particle diameter.

The Langmuir-Blodgett model
The Langmuir-Blodgett model treats the particle as a mass point, and considers only inertial disposition of the particle onto the bubble, neglecting its size. Langmuir and Blodgett derived an expression that relies solely on the Stokes number of the system:

$$P_{c-LB} = \left(\frac{\text{Stk}}{\text{Stk} + 0.2}\right)^2 \tag{2.13}$$

However, it should be taken into account that this model does not apply to small particles where collision occurs predominantly by interception and by Brownian diffusion, and inertial deposition is very weak [34]. Therefore, it is not applicable to the situation considered in this thesis.

The GSE-model
The GSE-model (for Generalised Sutherland Equation) is the model that applies to intermediate Stokes numbers, so $\text{Stk} \approx 1/12$. It is a very elaborate model that relies on (among others) the maximum possible collision angle, and takes into account both particle size and inertia. However, as will be shown in next section, this model is not necessary for the situation of this thesis and therefore will not be discussed here. For a detailed description of this model, the reader is directed to [34].

Collision models to be considered in this thesis
To investigate what model can be applied to the cases of this thesis, having a particle size in the order of hundreds of nanometers and a bubble size in the order of 10^{-4} to 10^{-3} m, the Stokes number is calculated. Writing equation (2.10) as a function of the particle settling velocity u_p, we obtain

$$\text{Stk} = \frac{d_p^2 u_p \rho_p}{9\mu d_b} \approx 10^{-5} u_p \tag{2.14}$$

Where we have taken, based on Polystyrene particles in 34.16 wt% water-sugar solution (as will be explained later), $\rho_p \approx 10^3$ kg/m^3 and $\mu \approx 10^{-3}$ Pa·s. It can very safely be assumed that the Stokes number of this system will be much less than $\frac{1}{12}$, as it is highly unlikely that u_p will be large enough to cause the Stokes number to come close to that value.

From this, we learn that the model that is applicable to the situations as considered in this thesis is the Sutherland-model, more precisely the Yoon-Luttrell model as the Reynolds number of the bubble falls into the intermediate regime. The particle-bubble collision efficiency in a bubble column can therefore be calculated using equation (2.12) and is, for a bubble diameter of 0.5 mm and a particle diameter of 100 nm, expected to be in the order of 10^{-7}.

Settling velocity

For the experiments in a bubble column, the settling velocity of the particles should be considered. It is determined based on theory from [37] and data from (mostly) [18] and (in one instance) [35]:

- Particle density (Mo): $\rho_p \approx 10^4$ kg/m^3

- Liquid density: $\rho_l \approx 10^3$ kg/m^3

- Particle diameter: $d_p \approx 10^{-7}$ m

- Bubble diameter: $d_b \approx 10^{-4}$ m

- Dynamic viscosity of the fluid: $\mu \approx 10^{-3}$ Pa·s

- Bubble rising velocity: $u_b \approx 10^{-2}$ m/s [35]

The settling velocity is an important quantity, for instance because particles that have sunk to the bottom of the flotation tube will settle on the bubble sparger in between the pores and are not available for flotation anymore. Depending on the Reynolds number, a variety of models can be used to evaluate the settling velocity. One of those models is the Stokes flow, which may be used for Re≪1 [37]:

$$u_p = \frac{(\rho_p - \rho_l)g d_p^2}{18\mu} \tag{2.15}$$

However, before this expression can be used, the particle Reynolds number in a bubble column as will be used in this thesis should be examined:

$$\text{Re}_p = \frac{\rho_l u_p d_p}{\mu} \approx 10^{-1} u_p \tag{2.16}$$

Which is much less than unity for velocities in the order of centimetres per second. Therefore the model for Stokes flow may be used in a bubble column, and it can be seen from equation (2.15) that the settling velocity of Molybdenum particles is in the order of tens to hundreds of nanometers per second, so not much over a millimeter per hour. From this, it may be concluded that Molybdenum nanoparticles sinking to the bottom in the experiment should not be a problem, except perhaps for the particles that are initially very close to the bubble sparger at the bottom of the setup, as they might deposit on the sparger due to settling. When using Polystyrene, settling becomes even less important since the density is roughly the same as that of water. In fact, the particles will (extremely slowly) drift upwards as the density of Polystyrene is just under that of the water-sugar solution.

Bubble-particle attachment

The probability of attachment of the particle to the bubble is dependent on a number of factors, most importantly the **collision angle** ϕ_c. This collision angle is defined as the polar angle between the very top of the bubble, and the point on the bubble where bubble and particle first meet. Once the bubble and the particle have collided, the particle will 'slide' down over the bubble surface, and at some point either leave the bubble surface again or find itself attached to it.

Whether or not the attachment of the particle to the bubble is successful has everything to do with the **adhesion angle** ϕ_a, the **maximum possible collision angle** $\phi_{\max}$, the **sliding time** t_s, and the **induction time** t_i. The sliding time is the time the particle spends sliding down from the point of attachment to the 'point of detachment' where the particle and the bubble separate again, which in the case of successful attachment is a hypothetical point. During this sliding time, three things must happen [38] for a successful attachment: 1) the liquid film between the particle and the bubble must thin down to a critical thickness, 2) the liquid film must rupture, creating a three-phase contact (TPC) line and 3) this TPC-line must grow to a stable radius. If the collision angle is greater than the adhesion angle, the sliding trajectory of the particle to the point of detachment, and thus the sliding time, is too short to allow for the full completion of these three processes and as a result the particle will not attach to the bubble. The induction time is the time needed for the completion of the three processes, and the adhesion angle ϕ_a is the collision angle for which $t_s = t_i$. The attachment probability can be seen as the ratio of the number of stream lines within the bubble trajectory that make the

particle collide with the bubble at an angle within ϕ_a, over the number of stream lines that make the particle collide with the bubble in general. This reduces to the simpler relation [36]:

$$P_a = \left(\frac{\sin\phi_a}{\sin\phi_{\max}} \right)^2 \tag{2.17}$$

Conveniently, Kouachi *et al.* [36] show that for small particles (in the sub-micrometer range), P_a goes to 1. This applies to the situations considered in this thesis. However, as mentioned earlier, they also note that the maximum possible collision angle can be smaller than 90°. A variety of models exist that give expressions for $\phi_{\max}$, for which the reader is directed to [36]. It is shown that for these models, P_a indeed gives lower values if $\phi_{\max}$ is not taken to be 90°. However, since the particle-size range in this thesis is in the order of 100 nm, this effect will not have a significant influence on the considered cases.

2.4.3. The complete flotation process in a Bubble Column

If the assumption is made that the bubble-particle aggregates are stable due to the small particle size, and that the number of already attached particles does not influence the probability of another particle attaching, a relatively straight-forward expression can be constructed that gives the relation between the extraction yield in a bubble column and the bubbling time. In this relation, the starting particle concentration is multiplied with the 'survival probability' to the power of the number of bubbles that pass through the column. In this survival probability, it is also taken into account what the probability is that the particle is in the region of the bubble column that is outside of the bubble trajectory.

$$P_{\text{Particle within bubble trajectory}} = \frac{A_{\text{bubble}}}{A_{\text{column}}} \tag{2.18}$$

$$N_{\text{Passed bubbles}}(t) = \frac{r_g}{V_B} t \tag{2.19}$$

r_g is the volumetric gas flow rate and V_B denotes the volume of one bubble. The resulting equation for the particle concentration after bubbling time t is given in equation (2.20). If the aforementioned assumptions hold, this relation is independent of the z-coordinate of the considered volume in the bubble column.

$$C_P(t) = C_P(0) \left(1 - \frac{A_{\text{bubble}}}{A_{\text{column}}} P \right)^{\frac{r_g}{V_B} t} \tag{2.20}$$

In equation (2.20), the particle concentration is denoted by C_P and P refers to the 'full' probability of particle-capture which is the product of the collision, attachment and one minus the detachment probability, in this case entirely given by equation 2.12 as the attachment probability is assumed 1, and the detachment probability is assumed 0. This equation assumes stationary liquid containing homogeneously dispersed particles, through which bubbles homogeneously flow: a bubble column. A prediction of the expected yield (defined as the amount of particles removed by flotation as a percentage of the initial concentration) in the experiment is shown in figure 2.8.
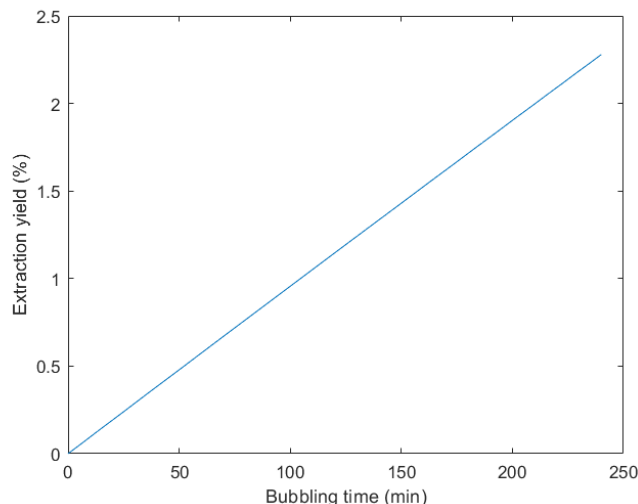
Figure 2.8: Prediction of the extraction yield from equation 2.20 with 500 nm particles and 0.5 mm bubbles and a volumetric gas flow rate of 5 sccm.

Due to the small particle sizes, the extraction efficiency is low. The model itself however seems to be reasonable, as especially for shorter times it matches well with Capelli's [18] results, even though it gives an overestimation for longer times, as shown in figure 2.9. This overestimation is not entirely surprising, as the model assumes both the attachment probability and one minus the detachment probability to be unity, which in reality only holds for sub-micron particles. The experimental results on the other hand are likely to be an underestimation, since it assumes a 100% recovery efficiency of floated particles, which will probably be lower due to sedimentation and (back-)flow effects. Also, it should be noted that the shapes of the curves are different: the experimental curve is in reality an adjusted fit, which assumes some maximum extraction efficiency, whereas the model assumes a 100% maximum extraction efficiency.
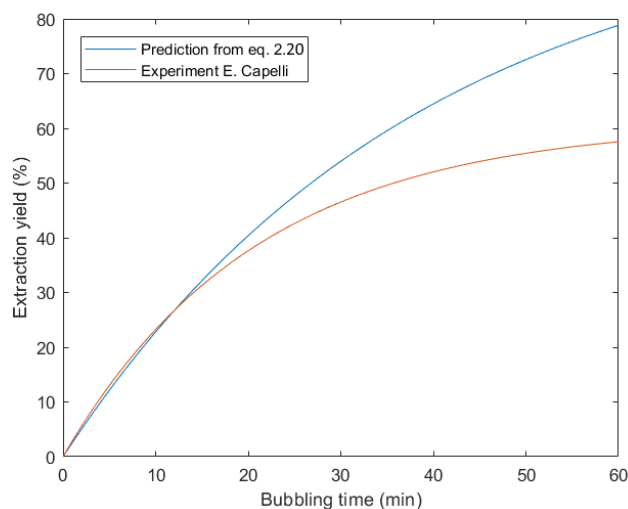
Figure 2.9: Equation 2.20 compared to experimental results from Capelli [18]. Here, a bubble column with 5 μm particles is considered, the bubble size is taken to be 0.65 mm and the gas flow rate is 25 sccm which matches Capelli's experiment.

When fluid flow is involved, the concentration will of course change in a different manner. If both the bubbles and the particles are flowing, thus have some velocity, the number of bubbles a particle encounters (per second, or over some trajectory) depends on the relative velocity. A more elaborate description of this approach will be given in section 4.1.2.

2.4.4. Void reactivity feedback effects when bubbling in a reactor

Having bubbles inside the reactor fuel of course has more effects on the reactor operation aside from the removal of fission products. Basically, when considering the larger scale, introducing bubbles into the reactor fuel means lowering the density. Every bubble is a place where there is no fissile material, so it can be expected that the reactivity feedback coefficient of the Helium bubbles in the fuel is negative. This effect was studied by Cervi *et al.* [39], who found that for a realistic bubble distribution as currently considered (taking the flow of the fuel and the location of bubble injection into account) the void reactivity feedback coefficient was in the range of approximately -340 to -330 pcm per percent void fraction, for void fractions of 0.437 to 1.308 percent.

2.5. Proposal for External Helium-Bubbling Facility

2.5.1. Design considerations

The Helium-Bubbling as it is currently viewed, will be done inside the reactor core, where the bubbles will flow with the salt. Afterwards, the gas is extracted. This poses the question: what about the particles that were attached to the bubbles? Currently, there is no worked-out design that takes care of the removal of floated particles in the MSFR.

Since for the efficiency of the flotation process it is important that particles and bubbles encounter each other as often as possible, it raises the question whether or not bubbling cocurrently with the stream is an effective approach. When the bubbles flow against the salt current for example, they will encounter much more particles, of course dependent on the flow conditions. This is not possible in the core (without considerable alterations to the reactor), but it is possible to achieve this in a separate Helium Bubbling Facility, connected to the salt flow loop and located outside of the reactor core. This allows for much more freedom with regard to the flow conditions, to maximise the efficiency of the fission product removal.

This translates into the following design proposal: the salt should flow into the facility from the top, and flow downward to exit the facility at the bottom. Near this bottom, Helium is introduced which flows upward through the salt, counter-current.

At the top of the facility, the salt surface level will be raised as a result of the introduction of Helium. The particles that are attached to the bubbles will be taken to the top of the salt, close to the salt surface level where they will be released. If nothing is done there, the particle concentration in the upper region of the salt will increase to some value, but the particles will not be removed from the salt. Therefore, an overflow should be introduced that causes the upper most portion of the salt to overflow out of the bubbling facility. On top of the facility, on the outside of the wall over which the overflow happens, an overflow-collector should be attached which can redirect the collected salt (with high particle concentration) to either re-processing or waste processing. This way, a small portion of the fuel salt is removed from the loop, but with it an increased fraction of the metallic particles. Since in this process froth might form, which is not part of the used computational methods, the overflow and removal of particle-rich salt from the Bubbling Facility is not worked out in this thesis.

2.5.2. Flow condition considerations

The gas should be able to flow towards the top of the facility. Therefore, the superficial salt flow rate must be kept below the bubble drift velocity. This means that this flow rate must be in the order of centimetres per second at most. Secondly, and related, the bubble size should be considered. In the MSRE, small and large bubbles are mentioned , the small ones being in the order of 0.01 inch (0.25 mm) [21]. These smaller bubbles are taken with the flow, whereas the larger bubbles float towards the surface. This latter property is what is needed in this design, so the bubble size should be chosen large enough so that the bubbles are actually able to float upwards against the current.

A third consideration that will prevent bubbles from exiting the facility at the bottom, is to give the Helium a high enough inlet velocity. The value of this inlet velocity partly relies on trial and error using OpenFOAM, as it introduces vorticity in the flow which might cause local velocities to exceed the maximum value for the chosen calculation time step causing the simulation to stop running.

2.5.3. The Design

Based on above considerations, the following design is proposed:
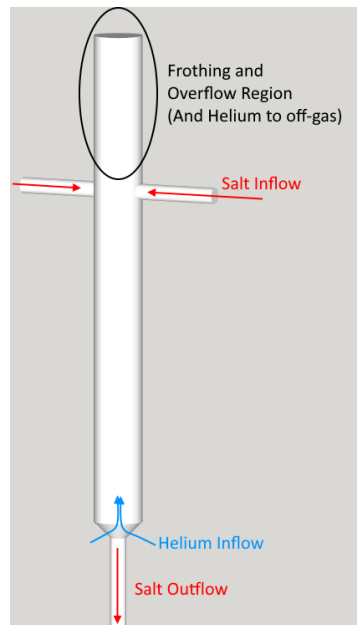
Figure 2.10: A 3D model of the proposed Helium Bubbling Facility.

Its diameter is 30 cm, the in- and outflow pipes have a 10 cm diameter. The height (from the top of the Helium inlet) to the bottom of the inlet pipes is 2 m. The upper most region, above the inlet channels, is where the Helium (with fission gases) is redirected to the off-gas system, and the frothing and overflow happens. The overflowing froth/salt, high in metallic fission products, is collected here. This part is not treated in this thesis.

3

Modelling in OpenFOAM

In this project, use is made of the 'twoPhaseEulerFoam'-solver for OpenFOAM. OpenFOAM is a widely used and well documented open-source CFD program. A very elaborate descritption of the modelling process and relevant equations can be found in Henrik Rusche's PhD thesis [40]. This report will stick to the basic equations and solution procedures used.

3.1. Governing equations

First and foremost, the equations for momentum and continuity should be considered. The phase continuity equation for phase κ reads:

$$\frac{\partial}{\partial t}(\alpha_\kappa \rho_\kappa) + \nabla \cdot (\alpha_\kappa \rho_\kappa \boldsymbol{U}_\kappa) = 0 \tag{3.1}$$

For the momentum, we start from the Cauchy-equation of momentum in conservative form:

$$\frac{\partial}{\partial t}\left(\rho \boldsymbol{u}\right) + \nabla \cdot \left(\rho \boldsymbol{u}\boldsymbol{u}^{\mathrm{T}}\right) = -\nabla p + \nabla \cdot \tau + \rho \boldsymbol{g} + \boldsymbol{F} \tag{3.2}$$

A number of things should be considered. Firstly, since a two phase flow is considered, the equation should be given an index κ to denote the phase it applies to. Secondly, since phase κ will have some phase volume fraction α_κ, we need to incorporate that too. As for the force term: this arises from the momentum transfer between the two phases, and therefore will be rewritten into a more suitable form: the inter-phase momentum transfer.

Furthermore, where in equation 3.2 τ is written, using the Boussinesq hypothesis[1] this can be written as the combined Reynolds (turbulent) and viscous stress. Taking all this into account and rearranging a bit, for phase κ this yields [40]:

$$\frac{\partial \alpha_\kappa \overline{\boldsymbol{U}}_\kappa}{\partial t} + \nabla \cdot \left(\alpha_\kappa \overline{\boldsymbol{U}}_\kappa \overline{\boldsymbol{U}}_\kappa^T\right) + \nabla \cdot \left(\alpha_\kappa \overline{\mathbf{R}}_\kappa^{\mathrm{eff}}\right) = -\frac{\alpha_\kappa}{\rho_\kappa}\nabla \overline{p} + \alpha_\kappa \boldsymbol{g} + \frac{\overline{\mathbf{M}}_\kappa}{\rho_\kappa} \tag{3.3}$$

In this equation[2], α denotes the volume fraction of the phase, $\overline{\boldsymbol{U}}$ the average phase velocity, $\overline{p}$ the average pressure, $\overline{\mathbf{R}}^{\mathrm{eff}}$ the average combined Reynolds and viscous stress, and $\overline{\mathbf{M}}$ the average inter-phase momentum transfer. The latter two will be explained further.

3.1.1. Combined Reynolds and Viscous Stress

In the Boussinesq hypothesis, the following expressions for τ from equation 3.2 hold:

---

[1]The Boussinesq hypothesis states that the momentum transfer caused by turbulent eddies can be modeled with an eddy viscosity [41].

[2]As is stated in Rusche's PhD thesis, usually, averaged conservation equations that describe averaged flow properties are solved in practical turbulence simulations.

$$\tau_{ij} = -\overline{\rho u_i' u_j'} \tag{3.4}$$

$$-\overline{\rho u_i' u_j'} = \mu_t \left(\frac{\partial U_i}{\partial x_j} + \frac{\partial U_j}{\partial x_i} - \frac{2}{3} \frac{\partial U_k}{\partial x_k} \delta_{ij} \right) - \frac{2}{3} \rho k \delta_{ij} \tag{3.5}$$

Where the term $\frac{\partial U_k}{\partial x_k} \delta_{ij}$ equals zero for incompressible fluids. This yields for $\overline{\mathbf{R}}_\kappa^{\text{eff}}$:

$$\overline{\mathbf{R}}_\kappa^{\text{eff}} = -\nu_\kappa^{\text{eff}} \left(\nabla \overline{\boldsymbol{U}}_\kappa + \nabla \overline{\boldsymbol{U}}_\kappa^{\text{T}} - \frac{2}{3} \mathbf{I} \nabla \cdot \overline{\boldsymbol{U}}_\kappa \right) + \frac{2}{3} \mathbf{I} k_\kappa \tag{3.6}$$

In these equations, u_i' is the acceleration in direction i, μ_t the eddy viscosity, U_i is the velocity component in diraction i, δ_{ij} the Kronecker delta, k the turbulent kinetic energy and ν_κ^{eff} the effective viscosity. $\nabla \boldsymbol{U}$ denotes the gradient of the tensor field $\boldsymbol{U}$.

3.1.2. Interphase Momentum Transfer

Due to the global conservation of momentum, the total sum of the momentum transfers over all phases should be zero. In the case of this thesis, there are only two phases, i.e. a continuous phase and a disperse phase. For such a two-phase system, a single expression for the momentum transfer to or from one phase to the other is sufficient to close the system. In that light, we define the Dispersed Phase Elements (DPE's). The momentum transfer to and from these DPE's (in practice: bubbles) will be considered. For the interphase momentum transfer in this approach, a number of contributions must be taken into account. These are:

- Drag;

- Lift; and

- Virtual mass.

As will be explained further on, averaging processes will lead to an additional contribution: the **Turbulent drag**.

Drag

There are numerous models that describe the drag of rising bubbles in a fluid. They are based on the following relation:

$$\boldsymbol{F}_d = \frac{1}{2} \rho A C_d |\boldsymbol{U}_r| \boldsymbol{U}_r \tag{3.7}$$

Where A denotes the frontal area and $\boldsymbol{U}_r$ the relative velocity of the bubble with respect to the continuous phase. C_d is the drag coefficient, for which the expression depends on the used drag model.

Rusche [40] proposes the use of the Schiller-Naumann drag model. In this model, the drag coefficient C_d is defined as [42]:

$$C_d = \begin{cases} \frac{24}{\text{Re}} \left(1 + 0.15 \text{Re}^{0.687} \right) & \text{Re} \leq 1000 \\ 0.44 & \text{Re} > 1000 \end{cases} \tag{3.8}$$

Lift

Following Auton (1987) [43], the lift force on a bubble in some liquid is described by the follwoing equation:

$$\boldsymbol{F}_l = C_l \rho V \boldsymbol{U}_r \times (\nabla \times \boldsymbol{U}_l) \tag{3.9}$$

Where C_l denotes the lift coefficient, ρ the density of the fluid, V the bubble volume and $\boldsymbol{U}_l$ the liquid velocity. In his research, Auton finds C_l to have a value of 0.5 [43]. However, Russche [40] states that the contribution of the lift force is negligible, and therefore sets C_l to zero. For clarity, the equation itself will still be shown in this chapter.

Virtual mass

The virtual mass term (also called 'Added Mass') originates from a virtual increase in mass as a result of the moving bubble taking some liquid with it. The virtual mass term determines the necessary work done by the moving bubble that is required for the change in kinetic energy of the fluid [44]. Russche [40] uses the following relation:

$$\boldsymbol{F}_{\mathrm{vm}} = C_{\mathrm{vm}}\rho V\left(\frac{D\boldsymbol{U}_l}{Dt} - \frac{D\boldsymbol{U}_b}{Dt}\right) \tag{3.10}$$

Where C_{vm} is the virtual mass coefficient, $\frac{D}{Dt}$ denotes the material derivative and $\boldsymbol{U}_b$ is the bubble velocity. Russche assigns to C_{vm} the value 0.5.

Turbulent drag

The Turbulent Drag term accounts for additional drag due to fluctuations of the dispersed phase [40]. Following Russche's interpretation of a paper by Gosman *et al* [45], it shows up as an extra term in the Inter Phase Momentum Transfer expression as a result of the derivation of the averaged momentum equations. For this reason, we look at this term only as part of the averaged inter-phase momentum transfer. It is given by:

$$\text{Turbulent Drag term of } \overline{\mathbf{M}} = -C_d\frac{3}{4}\frac{\rho}{d_b}\frac{v^t}{\sigma_l}|\overline{\boldsymbol{U}}_r|\nabla\alpha \tag{3.11}$$

In this equation, d_b denotes the bubble diameter, v^t the turbulent viscosity and σ_l the surface tension of the liquid.

Complete expression

Adding up all the terms from previous sections, we finally arrive at the expression for the inter-phase momentum transfer of phase b dispersed in phase l:

$$\begin{aligned}
\overline{\mathbf{M}}_b = {}& \alpha_b C_d \frac{3}{4}\frac{\rho_l}{d_b}|\overline{\boldsymbol{U}}_r|\overline{\boldsymbol{U}}_r \\
& + \alpha_b C_l \rho_l \overline{\boldsymbol{U}}_r \times \left(\nabla \times \overline{\boldsymbol{U}}_l\right) \\
& + \alpha_b C_{\mathrm{vm}} \rho_l \left(\frac{D\overline{\boldsymbol{U}}_l}{Dt} - \frac{D\overline{\boldsymbol{U}}_b}{Dt}\right) \\
& - C_d \frac{3}{4}\frac{\rho_l}{d_\kappa}\frac{v^t}{\sigma_b}|\overline{\boldsymbol{U}}_r|\nabla\alpha_b
\end{aligned} \tag{3.12}$$

Where it is worth noting that $\overline{\mathbf{M}}_b = -\overline{\mathbf{M}}_l$. This can be rewritten using multiplier terms A:

$$\begin{aligned}
\overline{\mathbf{M}}_b = {}& A_d \overline{\boldsymbol{U}}_r \\
& + A_l \overline{\boldsymbol{U}}_r \times \left(\nabla \times \overline{\boldsymbol{U}}_l\right) \\
& + A_{\mathrm{vm}} \left(\frac{D\overline{\boldsymbol{U}}_l}{Dt} - \frac{D\overline{\boldsymbol{U}}_b}{Dt}\right) \\
& - A_{td}\nabla\alpha_b
\end{aligned} \tag{3.13}$$

With this, the momentum equation can be constructed. Other equations that are included in the two-phase modelling include equations for the pressure and turbulence quantities, but since they are extensive and not necessarily relevant to discuss for the purposes of this thesis, the reader is directed towards Henrik Russche's PhD thesis [40].

3.2. Implementation in OpenFOAM

After the equations are discretized as treated by Russche [40], they can be implemented in the solver. The fields are then calculated according to following scheme:

1. Solve the phase continuity equation
2. Calculate the multiplier terms
3. Calculate the velocity fields without considering the pressure gradient
4. Solve the pressure equation
5. Correct the velocities with the new pressure eld, and update the phase fractions
6. Solve the transport equations for the turbulence quantities

Where of course the proper boundary equations and initial conditions must be chosen. These include 'No Slip'-boundary conditions on the walls of a geometry, and either fixed pressures or fixed velocities at inlets and outlets.

3.3. Meshing

The meshing is performed in 'blockMesh'. This gives a mesh with cuboid cells. To construct the mesh, the desired geometry has to be divided into 'boxes'. Every box should be a cuboid itself. Per box, the location in space of the vertices and the number of cells in each direction is specified. These boxes are then stitched together to generate the final mesh. In doing this, it is important to keep in mind that the cell faces on two sides of such a 'stitch' should coincide.

Within the mesh, the outer faces can be defined as 'walls' which allows for easy implementation of the boundary conditions. The same goes for any inlet or outlet faces. OpenFOAM has a built-in mesh checker as well.

4

Methodology

4.1. Numerical simulations

4.1.1. Benchmarking of the code

Before the twoPhasEulerFoam solver as described in previous sections can be used, it has to be benchmarked first. To this end, a bubble column experiment carried out by Harteveld [29] was computationally checked. In this experiment, a pseudo-2D bubble column was used that was 24.3 cm wide, 99 cm high, and 4.1 cm deep, with an initial water level of 70 cm. A superficial gas velocity of 2 cm/s at the inlet was chosen for the experiments.

At the bottom of this pseudo-2D column, air was introduced by means of a large array of needles. The needles uniformly covered the bottom of the column, and by selecting the needles through which air would or would not be introduced, the void fraction at the inlet could be set. The benchmarking in this case is done with the setup using all needles, corresponding to an inlet air phase fraction of 100% if one takes the close packing of the bubbles at the needle tips to approach a unity packing fraction. In the experiment, the bubble size was determined to be around 4 mm. In the simulations, the dispersed phase diameter will therefore be set to 4 mm.

Harteveld's setup was modeled using OpenFOAM's 'blockMesh' meshing tool, where 20 cells were used in the x-direction (width), 200 cells in the y-direction (height) and one in the z-direction (depth).
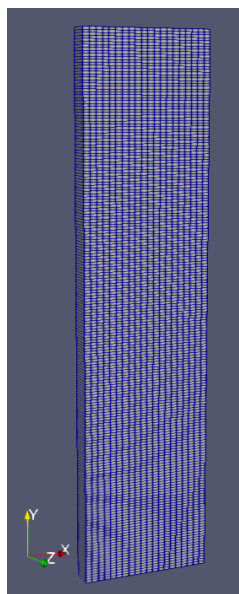

Figure 4.1: Mesh of Harteveld's pseudo-2D bubbling column.

4.1.2. Helium-Bubbling Facility simulations

Test case setup

After the code has been benchmarked, it can be used to do simulations on the facility as described in section 2.5. The Helium Bubbling Facility is modeled in 2D as shown in figure 4.2. The mesh is made of uniformly sized cells of 2 by 2 cm (in width and height), except for the lower part where the facility gets narrower and the Helium is introduced. In the conically shaped part, the cell width linearly decreases to one-third of its original width, which is the cell width in the outflow channel at the bottom.
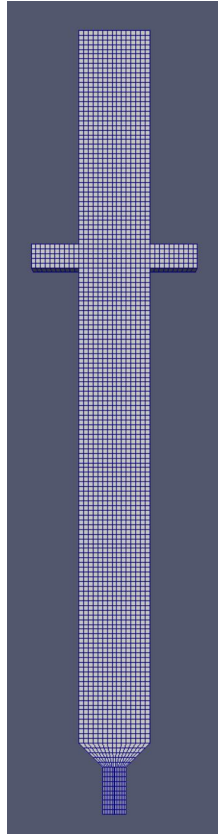

Figure 4.2: The 2D mesh used for the simulations on the Helium Bubbling facility.

Initially, the facility will be filled with fuel salt (with properties as described in section 4.2.1) to 10 cm above the top of the inflow channels. Helium will be introduced uniformly through the conical walls, normal to them. A helium volume fraction of 5% at the inlet will be used, with a Helium inlet velocity of approximately 28 cm/s, corresponding to both an x and y-component of the inlet velocity of 20 cm/s. At both salt inflow channels, the salt velocity will be 5 cm/s. This means that the outflow velocity of the salt will be set to 10 cm/s as the salt density is here taken to be constant.

From the MSRE reports [21] it was learned that the bubbles should be well over 0.01 inch in size, therefore here a uniform bubble size of 4 mm is set. In reality, the bubble size will likely not be uniform, nor will the bubbles be perfectly spherical, which they here are assumed to be. The way in which the Helium is introduced in reality, so for example through what kind of sparger, should be chosen such that the bubble size is suitable for this facility.

Calculation scheme: following streamlines

Two calculation schemes are investigated to draw conclusions on the extraction yield of the facility. First, after the local flow velocities and the void fraction values have been calculated for a certain snapshot in time, the salt velocities $\mathbf{u}_s$ are used to construct streamlines through the facility, from inlet to outlet. The particles that are to be removed are assumed to be of such small dimensions, that they will be carried by the salt current and thus follow salt stream lines. Using the salt velocities on this streamline, the particle's trajectory is also
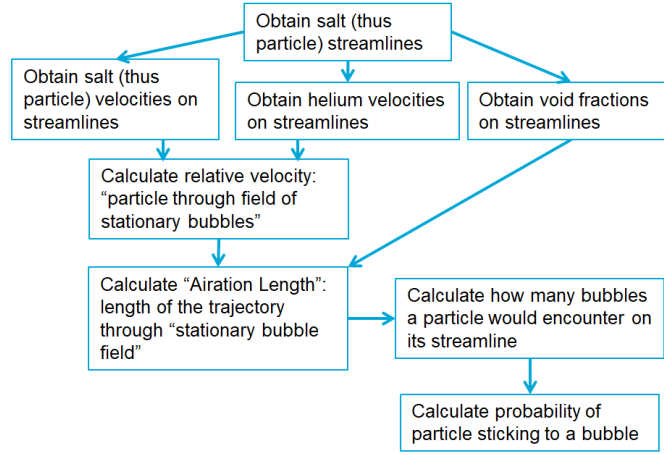
Figure 4.3: Schematic overview of the calculation scheme using particle streamlines.

'followed through time' as it is transported along this streamline. Next, the relative velocity $\mathbf{u}_r$ of the salt (and thus the particle) with respect to the helium is considered. This can be seen as the velocity with which the particle would be moving through a 'stationary bubble field'. Using the time scales calculated earlier, the **'Airation length'** L_a is calculated (although here we are using Helium rather than air), which is defined as "the distance a particle with velocity $\mathbf{u}_r$ would travel through a stationary bubble field in time Δt", where Δt denotes the time it takes the particle to go from the inlet to the outlet.

$$L_a = \sum_{n=1}^{N} (u_{s,n-1} - u_{g,n-1})(t_n - t_{n-1}) \tag{4.1}$$

In equation 4.1, n is the index for the point on the streamline with $n = N$ at the exit of the facility. The time t_n is the time at which the particle is at point n, calculated from the salt flow velocities and the spatial distances between the points on the streamlines up to point n. The airation length is then used in combination with the helium volume fractions on the streamlines to calculate the number of bubbles the particle will have encountered along it. Using the models for particle-bubble collision and attachment, we can finally calculate the particle extraction efficiency for salt flowing from the inlet to the outlet. This is done for a number of complete streamlines from a number of time snapshots from different times in the simulation.

Calculation scheme: full domain

Another method would be to consider not the particle streamlines, but the velocities and void fractions in the entire facility. By evaluating the salt velocity $\mathbf{u}_s$, the helium velocity $\mathbf{u}_h$ and the void fraction α_h at every cell, we can calculate how many bubbles a particle at that cell, at that moment, would encounter per unit of time. By applying the particle-bubble collision and attachment models to this, we can arrive at an average extraction yield per unit of time, which together with the average residence time of a volume of salt in the facility, would give the extraction yield for that volume after passing through the facility.
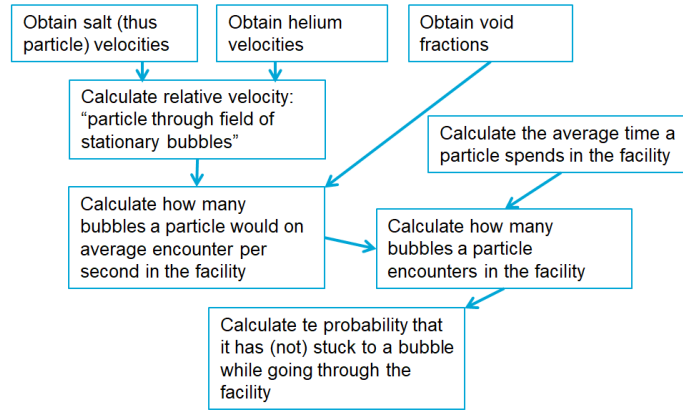
Figure 4.4: Schematic overview of the calculation scheme using the full facility domain.

4.2. Experiment on the verification of particle entrainment models

The particle collision and attachment models themselves should be investigated as well, preferably in conditions similar to those in the Molten Salt Reactor. Since it is in this stage neither possible nor particularly practical to perform experiments in actual Molten Salt Reactor Fuel, a simulant fluid is chosen to mimic the salt.

4.2.1. Selection of the fluid

The capture probability of the flotation process is strongly dependent on the motion of the fluid and velocity fields around the bubble. Through the Reynolds number, they are affected greatly by the kinematic viscosity of the fluid so for this reason, a simulant fluid should be chosen that has comparable kinematic viscosity. Based on work done by (among others) Capelli [18], a 41.1 wt% water-glycerol solution was initially thought to be suitable for these experiments as a substitute for the Molten Salt Reactor Fuel. However, as will be explained further on, polystyrene nano particles will be used in the experiments as well. Given that glycerol dissolves polystyrene, a simple water-sugar solution was chosen instead. In table 4.1, the properties of relevant fluids are shown.

Because other parameters such as the dynamic viscosity and the surface tension of a sugar-water solution differ from the Molten Salt values, the bubble formation in the simulant fluid will differ from the bubble formation in the fuel salt. Sugar solutions of different weight percentage were analysed to obtain the density and both the dynamic and the kinematic viscosity. It was found that a 34.16 wt% sugar-water solution has the desired kinematic viscosity and thus will be the simulant fluid of choice for experiments where the fuel salt needs to be mimicked.

As for the surface tension, though it does play an important role in flotation processes, no experiments were performed to measure the surface tension of the sugar solutions. Instead, the value is based on literature and taken to be 75 dyne/cm [46].

Table 4.1: Physical properties of molten salts and water at operational temperature T (K), density ρ (g/cm^3) , dynamic viscosity μ (mPa·s), kinematic viscosity ν (mm^2/s), surface tension σ (dyne/cm), Bond number Bo and Galileo number Ga. [18]

Fluids	T	ρ	μ	ν	σ	Bo	Ga
FLiNaK	900	2.018	3.594	1.781		10.92	309.16
LiF-ThF$_4$ (78-22 mol%)	900	4.418	7.622	1.725	~277	15.65	329.61
FLiBe (66-34 mol%)	900	1.707	7.524	4.408		8.92	50.48
MSBR fuel*	900	3.342	10.703	3.202	185	17.72	95.66
water	293	0.997	0.891	0.894	72.15	13.45	973.18
34.16 wt% Sugar-water solution	293	1.142	3.66	3.20	75		

*Reference composition: LiF-BeF-ThF$_4$ (72-16-12 mol%)

4.2.2. Selection of the particles

For the particles, the two things that are most important are the hydrophibicity and the size. If the particles are not hydrophobic (enough), they will not stick to the bubble surface and will therefore not be floated. Molybdenum is not only unwet by the fuel salt but is also hydrophobic, which makes it suitable for flotation experiments in water. This allowed Capelli [18] to use Molybdenum particles in her flotation experiments. Capelli also determined that the Molybdenum particles (that are created from fission at an atomic scale) in the fuel salt will agglomerate to particles with a size roughly up to half a micron [18]. Therefore, this (100 - 500 nm) will be the particle size range of interest in this experiment. In the experiments to be carried out in this thesis however, instead of Molybdenum particles, use will be made of fluorescent nanoparticles in the size range of interest. The reason for this is (as will be further explained in following sections) that in this research, the experiments revolve around the optical locating of the particles. Particles in this size range made of, for example Molybdenum, are too small for these methods. By using fluorescent particles, the light signals that the particles produce can be used to locate them. It is of course important that these particles are hydrophobic as well. For this reason, polystyrene fluorescent nanoparticles will be used as without surface agents, they are hydrophobic and will attach to bubble surfaces.

One might expect that the fact that polystyrene, the simulant particle material, and molybdenum, the 'real' particle material, have different densities will influence the relevance of the results. However, it is expected that both types of particles are sufficiently small so that the viscous forces of the fluid will dominate over the gravitational forces on the particles. Because of this, the expected settling velocity will be too low to have significant effects on the outcome of the experiment. It is not expected to cause problems for molybdenum, and even less so for polystyrene as its density is relatively close to that of water. Furthermore, as stated before, due to the small size and thus weight of the particles, the bubble-particle aggregates are expected to be stable (no detachment) and due to the great difference in size between the bubbles and the particles, the weight of the particles is also not expected to have a significant influence of the buoyancy of the bubble-particle aggregates.

4.2.3. Setup

In this experiment, the bubbling is done in a glass column with a diameter of 2.6 cm as shown in figure 4.5.
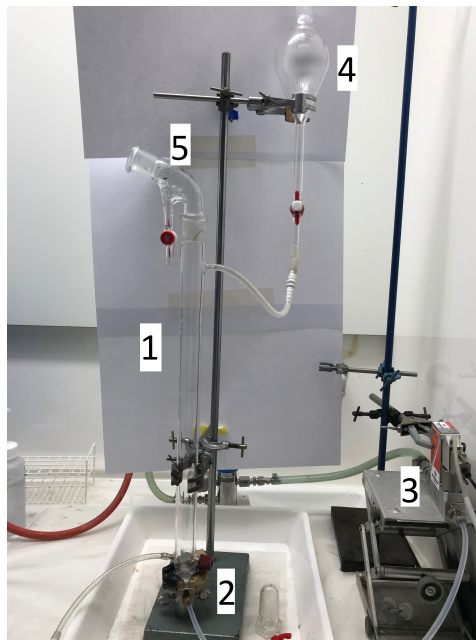

Figure 4.5: Picture of the setup with 1) the bubble column, 2) the bubble sparger, 3) the gas flow controller, 4) the fluid reservoir and 5) the Hallimond-tube.

The airflow is controlled through a Bornkhorst EL-Flow Select mass flow controller with a capacity of up to 500 sccm air (Standard Cubic Centimetre per Minute: cm^3/min air under standard conditions for pressure and temperature. This is the unit commonly used for gas flow controllers). The air is then let through a
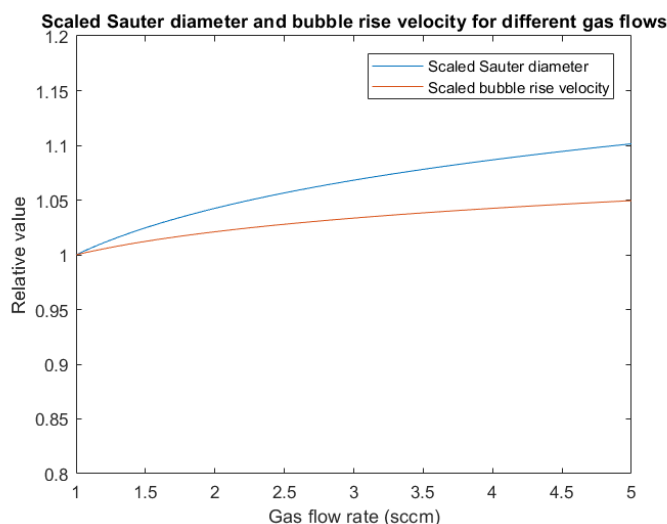
Figure 4.6: The relative Sauter diameter and bubble rise velocity for 1 to 5 sccm gas flows.

bubble sparger (metal sintered filter, SIKA-R3 with 26 mm diameter and a thickness of 3 mm and 3 μm pore size) at the bottom of the column where the bubbles are created. On top of the column, a Hallimond-tube is attached. The Hallimond-tube in this experiment is not used for the collection of particles but rather to make sure that the fluid level is far removed from the area of measurement to avoid influences of fluid circulation.

4.2.4. Method

The goal of this research is to learn how the bubbling affects the particle concentration within the fluid. Since the particles are too small to directly observe, Laser Induced Fluorescence (LIF) is used to examine the (relative) concentration of particles in a certain section of the column after set times of bubbling.

Because the aim is to obtain bubbly flow, it must be evaluated what gas flow rates are appropriate. The linear relationship between the gas holdup and the superficial gas velocity that holds in bubbly flow can be retraced to the requirement that the bubble size (and therefore terminal velocity) does not (significantly) change with the superficial gas velocity. Using equations 2.5, 2.6 and 3.8 we see that the Sauter diameter will change with approximately 10% over the 1 to 5 sccm gas flow rate range, and the change in bubble rise velocity will be under 5%. This is shown in figure 4.6. Since, following [29], bubble breakup and coalescence only start playing a role at relatively high gas flow rates, it is assumed that this does not play a role under the cicumstances considered in this experiment and thus that the bubble size is solely controlled by the sparger layout and the properties of the liquid and the gas flow. For that reason, it is assumed that the bubble size distribution for a given gas flow rate is narrow and that it varies only little with the gas flow rate, and that the bubble rise velocity changes even less, as shown in figure 4.6. This adds up to the conclusion that for gas flow rates lower than 5 sccm, the regime is expected to be bubbly.

Determination of bubble size

Relevant for the flotation process is the size of the bubbles. The bubble size distribution can be examined using photographic techniques, i.e. taking close-up pictures of the bubble column with a digital camera with a sufficiently high shutter speed as to minimise motion blur in the images. The images then were run through a MATLAB-script that was written by Capelli. The main steps that were performed to obtain the bubble size distribution are:

- Scale setting: make a scale based on the column with and exclude optically deformed sections at the column edge;

- Pre-processing: Substraction of the background to reduce noise and compensate for non-uniform illumination;

- Thresholding and watershed: The thresholding is done through what is called 'Otsu's method'. In a greyscale image, it evaluates every possible threshold for creating two classes (in this case: bubble and
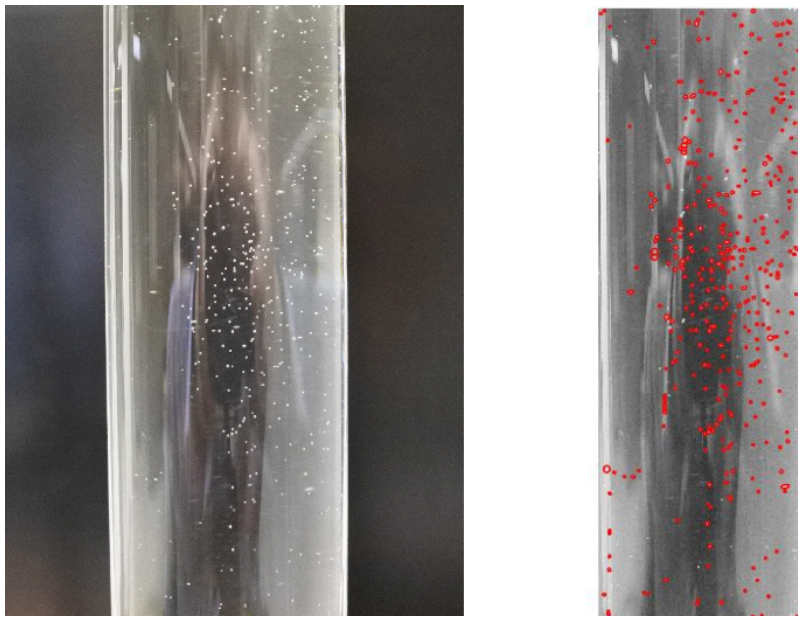
Figure 4.7: An original image of the bubbles in the column (left) next to the processed image (right). The recognised bubbles are encircled.

not-bubble). The chosen threshold is where the variance within a class is minimal and the variance between the classes is maximal. To separate overlapping bubbles, a watershed-transform is used. This technique treats a grayscale image as if it were a 3D map, where the brightness of a pixel denotes the height. The watershed process then traces the peaks of 'ridges' to separate different (adjacent) 'puddles', in our case the bubbles.

- Ellipse fit and extraction of the dimensions.

An example of an original photograph and the processed image with the bubbles found and encircled by the program is given in figure 4.7.

Two-coloured Laser Induced Fluorescence

In the fluid, two types of nanoparticles are present. One that is suitable for flotation (i.e. hydrophobic) and another that is as similar as possible, but unsuitable for flotation (i.e. hydrophilic). This way, a distinction can be made between what is an effect of actual flotation, effects of other events, such as fluid circulation due to the bubble flow. The two particle-types (hydrophobic SPHERO Nile Red fluorescent polystyrene particles without surface groups, 0.1-0.3 μm and hydrophilic Lab261 Orange fluorescent polystyrene nanoparticles with NH_2 surface groups, 0.2 μm) have the same excitation wavelength, but their emission spectra differ so that the particle concentration of both particles can be examined separately. These particles are homogeneously suspended in the flotation column and then illuminated by a 532 nm laser light source, which is at the excitation peak of the particles. The particles then will emit light in their respective emission spectra, which can be detected by a LIF-detector camera. The amount of detected light from both emission spectra can then be used to calculate the flotation efficiency within the bubble column. Figure 4.8 gives a schematic representation of the fluorescence measurements.
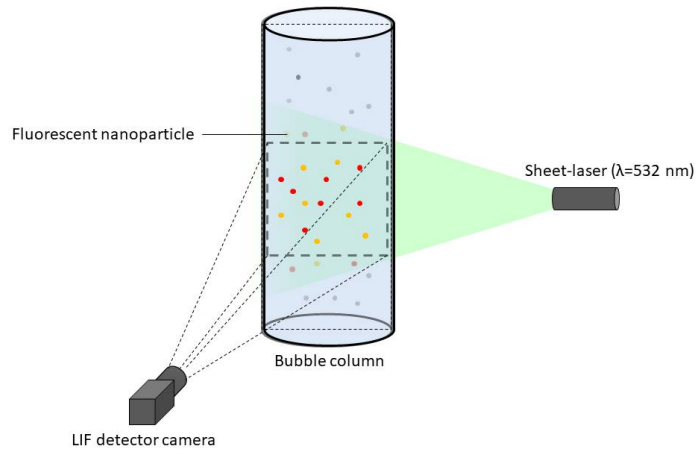
Figure 4.8: A schematic overview of the fluorescence measurements. The green arrows represent green light incident on the fluorescent particles, that due to this emit red light in all directions represented by the red arrows.
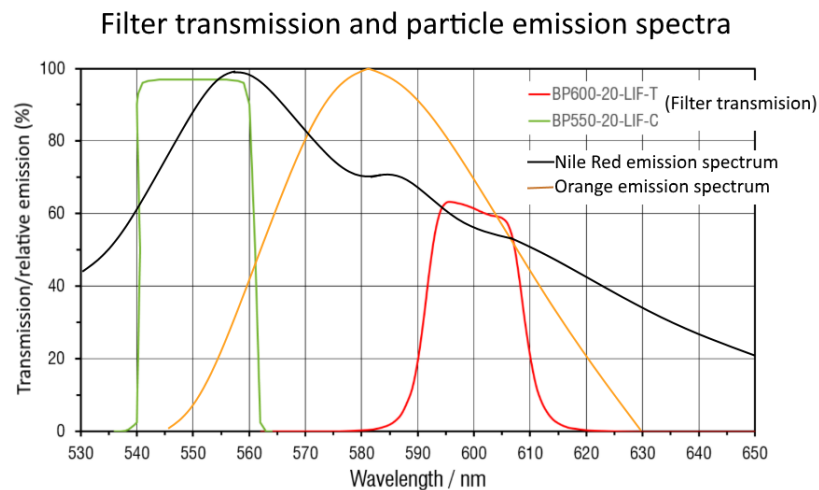

Figure 4.9: The transmission curve of the LIF-filter, together with the emission spectra of the particles.

The filter that is used in the two-coloured LIF setup is shown in figure 4.9, together with the emission spectra of the particles. The peaks in this filter do not exactly overlap with the emission peaks of the particles, especially not the orange one, but since the overlap between those two spectra is still relatively large, it is assumed (and later tested) that this setup still works. In the wavelength-range from 540 to 545 nm, it can be seen that the emission of the orange particle is (practically) zero. This means that whatever fluorescence signal is detected in this wavelength range, has to come from the Nile Red particles. This fact, together with the relative intensities shown in both the emission and filter spectra, can be used to assess what part of the fluorescence signal at 600 nm is coming from what particle. This way the Orange and Red signals can be separated which allows us to isolate the effects of flotation on the concentration from other effects.

<div style="text-align: right; font-size: 3em;">5</div>

Results

5.1. Results of computational simulations

5.1.1. Benchmarking results

For the benchmarking, the local void fractions and water velocities were calculated using the twoPhaseEulerFoam-solver, and the results are compared to the experimental findings of Harteveld [29]. Reasonable agreement is achieved in both the flow velocities and the void fractions. The local void fractions at the height of **0.7 m** above the sparger give somewhat lower numbers than measured in the experiment, but the average void fraction at that height (about 7%) does present a good match to what was mentioned by Harteveld in his experiments for the total volume averaged void fraction [29]. It appears that the computational method gives a more homogeneous bubble distribution throughout the column height than the experiment does, which could be the result of numerous effects, such as bubble-bubble interactions or wall-effects not included in the code.
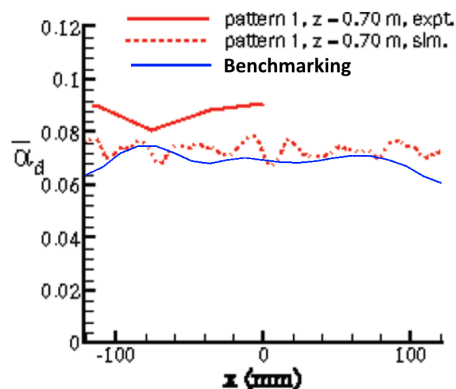

Figure 5.1: Results of the benchmarking of Harteveld's experiment (in blue), superimposed on a figure from Monahan *et al* [47]. The red-dotted line is a result of another simulation, done by Monahan.

As for the average fluid velocities, the results are shown in figure 5.2.

It can be seen that there is a significant difference in the shape of the velocity profile, as shown in orange in figure 5.2. Where Harteveld's velocity profile seems relatively uniform, from the simulations it seems that there is downflow of water along the walls and upflow along the middle. This corresponds to the (slightly) higher void fraction in the middle as compared to near the walls as seen in figure 5.1. In Harteveld's experiments (see figure 5.1), the void fraction near the walls appears not to be lower than in the middle, except perhaps *very* close to the walls, giving a more uniform water velocity profile. What is also worth noticing, is that contrary to the benchmarking results, the average axial water velocity in Harteveld's experiment is clearly nonzero, implying a nonzero net water flow upwards. Harteveld mentions that this is likely due to a bias in the velocity measurements [29].
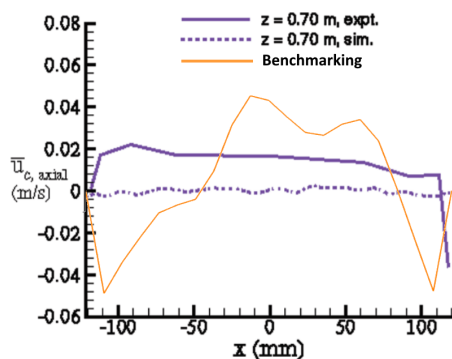
Figure 5.2: In orange the results of the benchmarking of the axial fluid velocity in Harteveld's experiment, superimposed onto a figure from Monahan *et al* [47]. The dotted line is the same Mohanan study.

5.1.2. Results of extraction yield calculations for the Helium Bubbling Facility

Using streamline tracking

For the tracing of the streamlines, at five separate times, three separate groups of streamlines were considered: after (approximately) one, two, three, four and five minutes of bubbling, streamlines beginning at the left inlet, streamlines beginning at the right inlet, and streamlines ending at the outlet were considered. This lead to fifteen separate groups of streamlines. Only streamlines that go all the way from inlet to outlet are considered. In figure 5.3, an example of the simulation results for the streamlines is shown.
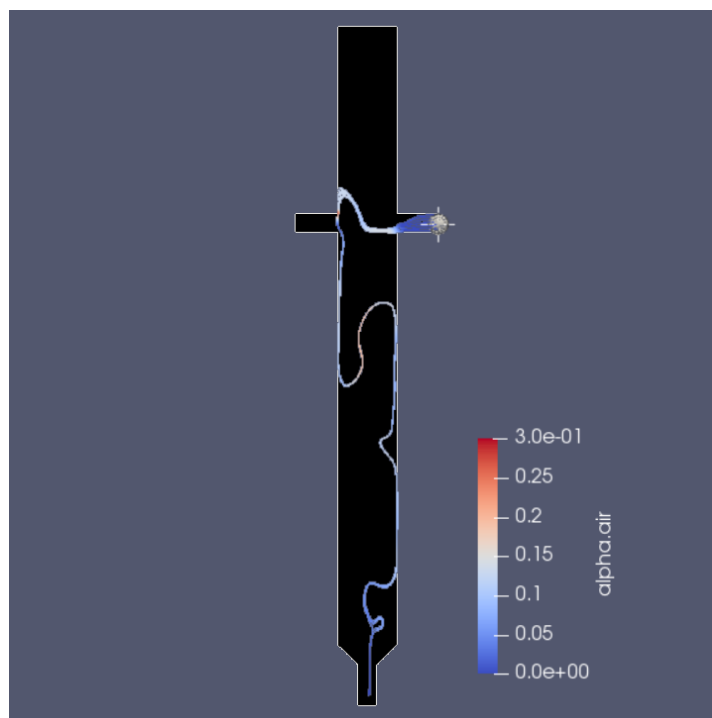
Figure 5.3: An example streamline group, at 48 seconds. The seed is at the right inlet.

Since the streamlines going all the way from inlet to outlet tend to be very closely grouped together and almost identical, one streamline from each of the fifteen groups was used for calculations. In table 5.1, the results are displayed, along with the resulting extraction efficiency for 0.5 μm, 1 μm, 10 μm and 100 μm particles ($\eta_{0.5}$, η_1, η_{10} and η_{100}, respectively) which follow from the earlier discussed Yoon-Luttrell model (equation 2.12). The larger particle sizes are included to illustrate the significant effect the particle size has on the extraction efficiency. This effect is at a maximum in the range of 10 to 200 μm [33], after which the negative effects of the greater size have a greater influence on the flotability.

Table 5.1: The results for the fifteen streamline groups. N is the number of bubbles a particle would encounter along this streamline, L_s is the length of the streamline, L_a is the previously introduced Airation Length. η_D denotes the extraction efficiencies for D µm particles.

Time (s)	Seed location	N	L_s (m)	L_a (m)	$\eta_{0.5}$ (%)	η_1 (%)	η_{10} (%)	η_{100} (%)
55	Left	37	2.78	2.52	$1.1 \cdot 10^{-3}$	$4.3 \cdot 10^{-3}$	$4.3 \cdot 10^{-1}$	35.0
63	Right	117	5.23	4.93	$3.3 \cdot 10^{-3}$	$1.3 \cdot 10^{-2}$	1.3	73.8
64	Bottom	75	2.55	2.91	$2.1 \cdot 10^{-3}$	$8.5 \cdot 10^{-3}$	$8.5 \cdot 10^{-1}$	57.5
129	Left	44	2.89	6.13	$1.5 \cdot 10^{-3}$	$6.1 \cdot 10^{-3}$	$6.0 \cdot 10^{-1}$	45.7
124	Right	65	3.31	4.05	$1.9 \cdot 10^{-3}$	$7.5 \cdot 10^{-3}$	$7.5 \cdot 10^{-1}$	53.0
123	Bottom	77	2.95	2.73	$2.2 \cdot 10^{-3}$	$8.9 \cdot 10^{-3}$	$8.8 \cdot 10^{-1}$	59.0
186	Left	38	2.71	2.57	$1.1 \cdot 10^{-3}$	$4.3 \cdot 10^{-3}$	$4.3 \cdot 10^{-1}$	35.3
191	Right	77	4.10	4.67	$2.2 \cdot 10^{-3}$	$8.8 \cdot 10^{-3}$	$8.8 \cdot 10^{-1}$	58.8
186	Bottom	40	2.82	2.86	$1.1 \cdot 10^{-3}$	$4.6 \cdot 10^{-3}$	$4.6 \cdot 10^{-1}$	36.8
224	Left	56	2.79	2.52	$1.6 \cdot 10^{-3}$	$6.5 \cdot 10^{-3}$	$6.5 \cdot 10^{-1}$	48.0
253	Right	83	4.14	4.22	$2.4 \cdot 10^{-3}$	$9.7 \cdot 10^{-3}$	$9.6 \cdot 10^{-1}$	62.2
246	Bottom	36	2.84	2.81	$1.0 \cdot 10^{-3}$	$4.1 \cdot 10^{-3}$	$4.1 \cdot 10^{-1}$	33.7
293	Left	48	2.86	2.16	$1.4 \cdot 10^{-3}$	$5.5 \cdot 10^{-3}$	$5.5 \cdot 10^{-1}$	42.6
300	Right	83	3.50	5.14	$2.4 \cdot 10^{-3}$	$9.5 \cdot 10^{-3}$	$9.4 \cdot 10^{-1}$	61.4
299	Bottom	77	3.57	4.10	$2.2 \cdot 10^{-3}$	$8.8 \cdot 10^{-3}$	$8.8 \cdot 10^{-1}$	58.9
	Average	**64**	**3.27**	**3.62**	**0.0018%**	**0.0074%**	**0.73%**	**50.8%**

From table 5.1, the effect of the counter-current bubbling can be recognised, since the Airation Length is on average approximately 11% greater than the actual length of the streamline.

Using all field values

As mentioned in section 4.1.2, another way of calculating the extraction yield would be to not follow streamlines, but to look at the entire domain of the facility. Because the region above the salt surface must be excluded, only a certain section of the facility is taken into account which is shown in figure 5.4.
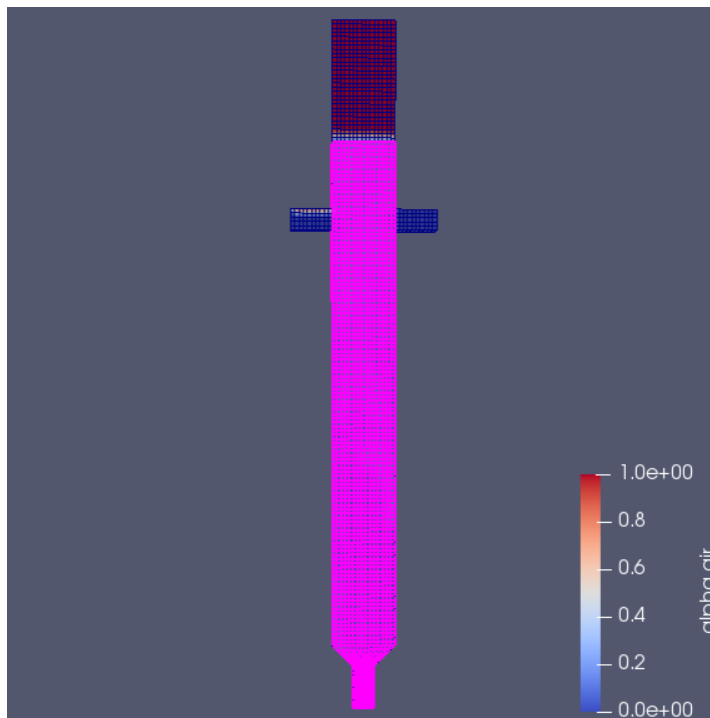

Figure 5.4: The domain for the full-facility calculations. Only the pink cells are considered.

A short recap of what is calculated here: for every cell, the relative velocity of the salt (thus particles) with respect to the bubbles is calculated. Multiplying the resulting 'distance per second' with the local void fraction

and dividing it by the bubble size gives the average number of bubbles passing a particle in this cell per second. Since both the flow velocity through the in- and outlet and the salt volume in the facility are known, the average amount of time a volume of salt stays in the (2D) facility can be calculated by dividing the (2D) volume of the facility over the out(/in)flow velocity, and equals 70 seconds. These two values combined gives the number of bubbles a particle will on average encounter during its stay in the facility, which together with the Yoon-Luttrell model can be used to calculate the extraction yield.

Table 5.2: The results of the extraction efficiency calculations using the full facility domain. The values are averaged over the entire volume, dN denotes the number of bubbles a particle encounters per second.

Time (min)	$\overline{dN}$ (s^{-1})	$\overline{\eta_{0.5}}$	$\overline{\eta_1}$	$\overline{\eta_{10}}$	$\overline{\eta_{100}}$
1	6.5	0.013%	0.051%	4.9%	90.1%
2	6.0	0.012%	0.048%	4.6%	90.7%
3	5.7	0.011%	0.045%	4.4%	88.9%
4	5.6	0.011%	0.045%	4.3%	89.3%
5	5.6	0.011%	0.044%	4.3%	90.0%
Average	**5.9 s^{-1}**	**0.012%**	**0.047%**	**4.5%**	**89.8%**

The results from the two approaches is shown in figure 5.5. It can be seen that the volume averaged approach gives higher extraction efficiencies. The volume averaged void fraction in the facility under these circumstances was calculated to be 9%, which, following section 2.4.4, would mean that this causes a reactivity decrease of approximately 3%.
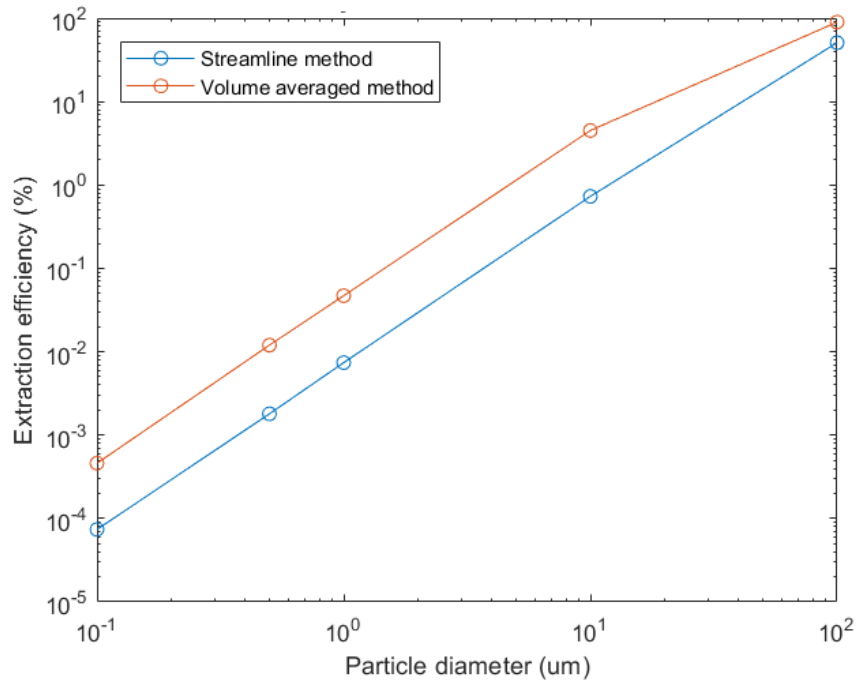

Figure 5.5: Comparison of the results from the two approaches. In blue, the extraction efficiencies calculated from following particle streamlines and in orange, the extraction efficiencies calculated from considering the entire domain.

5.2. Preliminary results for the experiments

5.2.1. Measurements on potential simulant fluids

As mentioned before, Glycerol-water solutions are not compatible with polystyrene particles so a simple sugar-water solution is chosen instead. Since it is preferable that the simulant fluid has the same (or similar) kinematic viscosity as the MSFR-fuel, the viscosities and densities of several sugar-concentrations are measured. See table 5.3 and figure 5.6.

Table 5.3: Properties of sugar-water solutions, experimentally determined as part of this research.

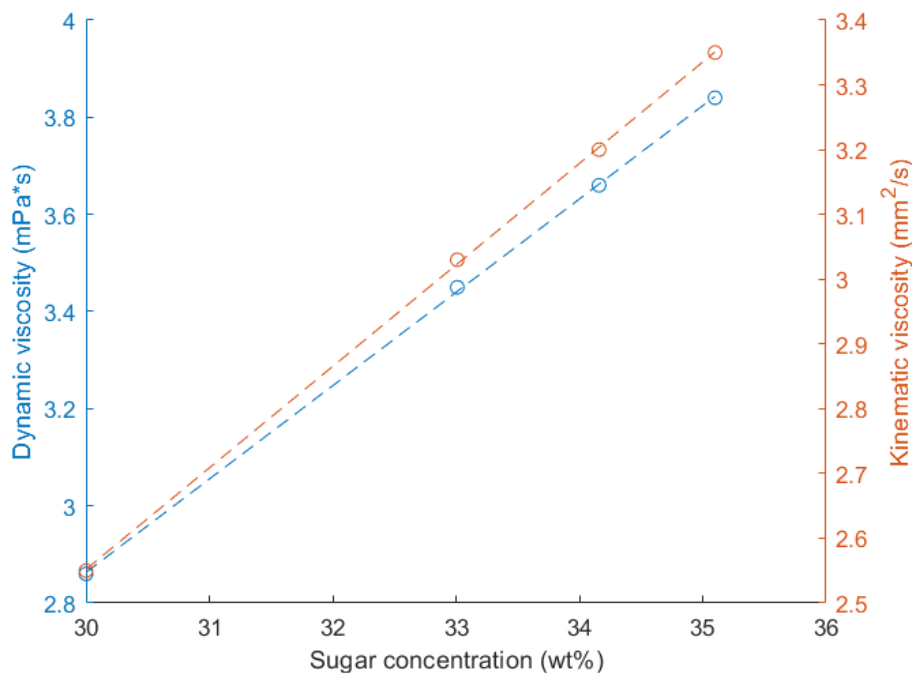| Sugar wt%	ρ (g/cm^3)	μ (mPa·s)	ν (mm^2/s)
30.00	1.123	2.86	2.55
33.01	1.138	3.45	3.03
34.16	1.142	3.66	3.20
35.10	1.145	3.84	3.55

Figure 5.6: Viscosities of some concentrations of sugar-water solutions following table 5.3.

As mentioned before, the 34.16 wt% concentration has the desired kinematic viscosity and will thus be the simulant fluid in the experiments.

5.2.2. Flow regime

Previously, it was mentioned that it is preferred the experiments are conducted in the homogeneous flow regime. In this regime, there is a linear relationship between the gas holdup and the superficial gas velocity. First, this was examined using regular de-ionised water. See table 5.4.

Table 5.4: Values for the gas holdup for various gas flow rates in water.

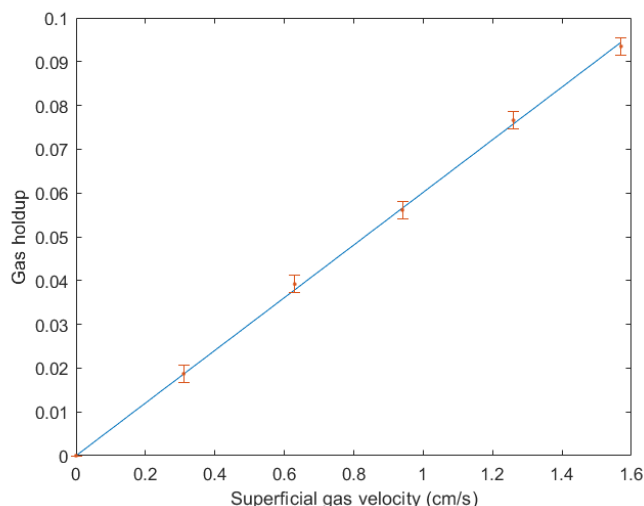| Gas flow rate (sccm)	Superficial gas velocity (cm/s)	Gas holdup ε_G ($\cdot 10^{-2}$)
100	0.31	1.87
200	0.63	3.92
300	0.94	5.61
400	1.26	7.66
500	1.57	9.35

Figure 5.7: The measured gas holdup in water for various superficial gas velocities, along with a linear fit.

As can be seen from figure 5.7, we can indeed recognise a linear relationship between the gas holdup and the superficial gas velocity and can therefore state that here we are in the homogeneous (bubbly flow) regime. As for the simulant fluid, a 34.16 wt% water-sugar solution, things are not necessarily the same.

In the simulant fluid (the water-sugar solution), there are significantly more bubbles present in the column at any given moment, due to their lower rising velocity which is a result of the higher viscosity. The presence of these very numerous, very small bubbles makes the setup unfit for LIF at higher gas flow rates. Because of this, the gas flow rate will be kept at values under 5 sccm. At gas flows in this range, it was found that the gas holdup is much too small to perform meaningful measurements on. In other words: the total volume of bubbles within the column is so small that the surface level of the solution doesn't rise enough to measure accurately. This prevents us from using above method to assess the flow regime that we are in. However, at these (low) gas flows the individual bubbles are small (and thus slow) enough to track with the eye. This way, one can visually determine whether or not the flow can be considered homogeneous. According to theory described in previous sections, this is the case when there is no significant large scale circulation of bubbles within the column. From gas flows of 4 sccm and higher, it can be seen that the bubble flow becomes turbulent and some bubbles are indeed travelling downward. These are strong indications that we are no longer in the bubbly flow regime and thus gas flows should be kept under 4 sccm.

5.2.3. Bubble dimensions

As described in the Methodology-chapter, bubble dimensions were determined based on photographs of the bubble column. For different gas flow rates in the range from 1 to 4 sccm, several pictures were taken from which the average bubble diameter is calculated. These measurements were done in the simulant fluid.

1 sccm

For the 1 sccm gas flow, the results on the bubble size measurements are displayed in table 5.5 and figure 5.8. The average equivalent diameter of the bubbles was found to be 0.291 mm with an average standard deviation of 0.094 mm.

2 to 4 sccm

These experiments unfortunately could not be carried out, as the 2020 Corona-crisis caused the university to prohibit experimental work by students. They are therefore left as a recommendation to be carried out in future research.
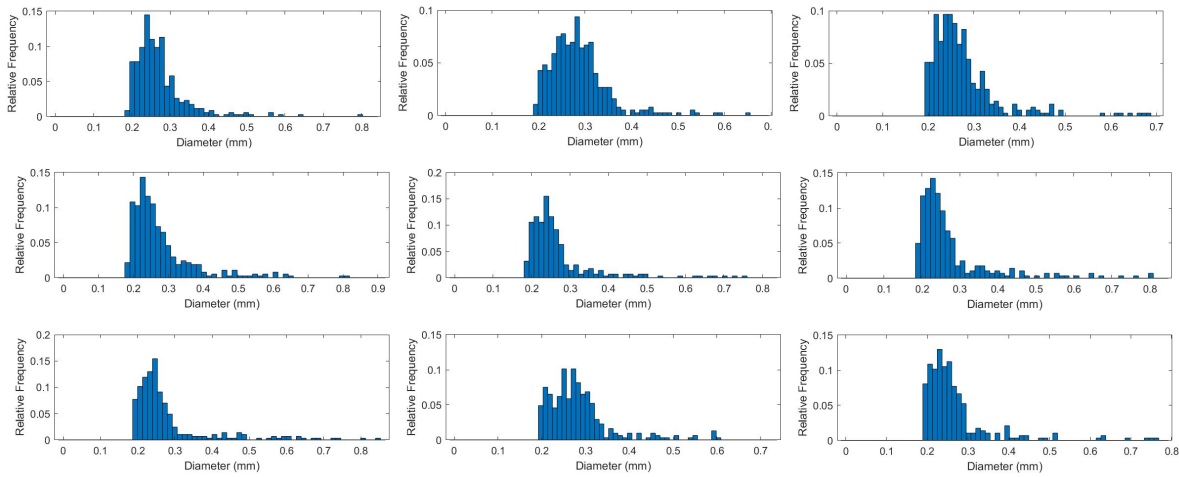
Figure 5.8: The results of the bubble size determination of nine images of the bubble column at a gas flow of 1 sccm in the simulant fluid.

Table 5.5: Average equivalent diameter (ED), Sauter diameter (SD) and volume diameter (VD) as determined from nine photographs at a gas flow of 1 sccm in the simulant fluid.

Picture	Number of bubbles	Avg. ED (mm)	Avg. SD (mm)	Avg. VD (mm)	ED Standard Deviation (mm)
1	345	0.287	0.343	0.401	0.078
2	373	0.299	0.340	0.374	0.071
3	352	0.287	0.345	0.394	0.080
4	370	0.294	0.383	0.463	0.100
5	284	0.288	0.401	0.502	0.109
6	281	0.290	0.402	0.497	0.111
7	285	0.298	0.420	0.516	0.119
8	306	0.297	0.348	0.389	0.078
9	285	0.284	0.380	0.471	0.100
Average	**320**	**0.291**	**0.374**	**0.445**	**0.094**

5.3. Results of measurements using Laser Induced Fluorescence

As mentioned above, the 2020 Corona-crisis caused further experiments to be cancelled across the University. For this reason, the LIF experiments have not been carried out, nor has the set-up even been built or tested. Therefore, like above experiments, the LIF-experiments are left as a recommendation for future students or researchers to perform.

6

Discussion, conclusions and recommendations

6.1. Discussion

6.1.1. Numerical simulations

Error in CFD prediction

The simulations were run using the twoPhaseEulerFOAM solver for OpenFOAM. Even though the PhD thesis of Henrik Russche [40] provides a lot of insight into the physics behind it, some aspects remain to be investigated, such as the uncertainties in the CFD predictions. A common method to investigate the uncertainties is by performing grid refinement studies on the simulations, but these were not carried out in this thesis, not in the last place due to a lack of computational power and time. Because of this, no error bars or margins were included in the results from the simulation.

2D versus 3D

The simulations were carried out in 2D, which obviously does not perfectly match the 'real' 3D facility. Although it has been reported that (at least for small (15 cm) diameter bubble columns) 2D simulations give good agreement for axial liquid velocities and fractional gas holdup, a 3D simulation is needed to accurately model eddy diffusivity and axial dispersion, according to Ekambara *et al* [48]. In that study, it is explained that this effect is likely caused by the restriction of the directions for convection currents in 2D simulations. As for this thesis, a 3D simulation would allow for the investigation of the influence of different modes of axial symmetry (with regard to the number of inlet pipes).

Validity of attachment models

A third subject for discussion is the validity of the attachment models. The ones mentioned in the theory are said to be valid for the considered situations, but it would be good to test their validity experimentally. Unfortunately, due to the 2020 Corona-crisis these experiments could not be carried out. Also, since the focus in this research was mainly on the sub-micron range (which was also going to be the subject of the experiments), not a lot of attention has been paid to attachment (or detachment) models that play a role for larger particles. Bubble-particle aggregates are said to be stable for sub-micron particles, but as they get larger, the (initially assumed nonzero) detachment probability will grow and start to have a negative influence on the extraction efficiency.

Validity of the 'particles-following-streamlines' assumption

Likewise, as particles get larger, the original (and important) assumption that particles follow the streamlines will no longer hold, and again other models will apply. More importantly, for this reason the numerical 'streamline-approach' used in this thesis will no longer be suitable since it takes particle streamlines to be identical to salt streamlines, and thus for this a three-phase method should be used instead for more accurate predictions.

Difference between the two approaches

The calculated efficiencies are significantly higher in the full-volume approach than they are in the streamline-following approach. This of course makes sense, since the salt in the facility has an average residence time of 70 seconds, and the tracked streamlines lead from inlet to outlet in as little as 10 to 20 seconds. This is because OpenFOAMs streamline-tracking is terminated after a set minimal velocity, leaving only a couple of streamlines that go all the way from inlet to outlet. These correspond to the 'fastest' particles, i.e. those that stay in the facility much shorter than the average. In the full-volume approach, there is the implicit assumption that the particle distribution is homogeneous throughout the facility. In reality, the concentrations are related to the flow profiles and the local extraction rate and therefore likely not homogeneous. This will lead to an overestimation of the extraction efficiency in the case that local concentrations are lower in regions with higher void fractions, which is where extraction rates are highest. This is a reasonable assumption, as in this research the void fractions were only used for the calculation of the number of bubbles a particle would encounter, and not for the adjustment of the local particle concentration. This effect should therefore be taken into account in future research concerning the Helium Bubbling Facility.

6.1.2. Experiments on flotation models

Bubble size determination

One of the first experiments carried out in this thesis was the determination of the bubble size. What became apparent after studying literature, is that the found average Sauter diameter of the bubbles at a gas flow of 1 sccm was 0.37 mm, which is much smaller than the 1.2 mm that was expected from equation 2.5. This raises the question whether or not equation 2.5 holds for very small pore sizes. Since changing any of the parameters has a very small effect on the outcome, it is unlikely that (a combination of) measurement errors (in ρ or μ) or incorrect assumptions (in σ, d_p or J_g) have lead to this difference. It seems more likely that the factor of 7.35 is not a constant over the entire range of pore sizes, but has a different value for more extreme cases.

A large part of the experiments on bubble sizes could unfortunately not be carried out due to the 2020 Corona-crisis. However, another problem hindered the experiments as well. At some point, it became apparent that the sparger did not seal off the entire inside of the column walls completely, allowing air to pass the sparger along the sides, instead of going through it.
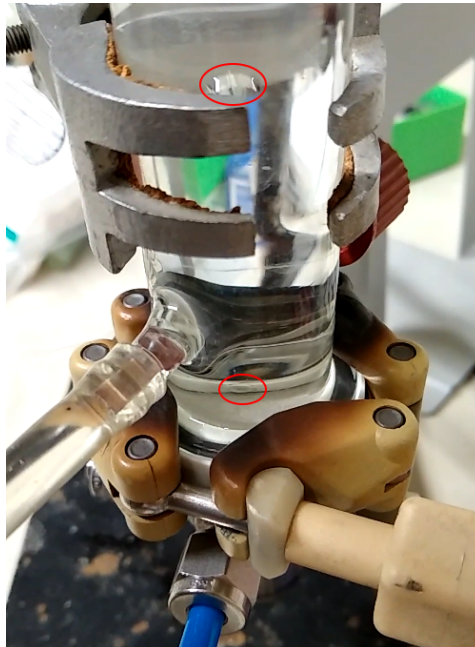

Figure 6.1: Close-up of the bottom part of the flotation column. Two bubbles can be seen: one at the top, that has just crept past the sparger some moments before, and one bubble that is in the process of creeping past it. Also note that even though a (small) gas flow rate is set, no air is actually going through the sparger.

These bubbles did not come from the sparger and therefore have vastly different dimensions. They are much

larger than the bubbles from the sparger, and therefore rise quicker and introduce relatively strong flows in the column. This issue was 'fixed' using a makeshift rubber seal, crafted from a part of a cut-off finger of a rubber glove which was placed around the sparger. This worked relatively well, but was no sustainable solution. Also, bubbles tended to stick to the rubber for some moments, which caused some bubble coalescence which obscured measurements of the 'true' bubble size caused by the sparger.

Controlling the gas flow rate
Since the air chamber under the bubble sparger is relatively large, it takes a long time at low gas flows for the pressure to build up to the point where the air is pressed through the sparger. Because of this delay, even though the air flow controller worked well, it was difficult to exactly tune the air flow that actually went through the sparger. Furthermore, because of the large size of the previously described bubbles that creep past the side of the sparger, they contain a significant fraction of the set air inflow rate. This further complicates precise control over the gas flow through the bubble column.

6.2. Main conclusions
In this research, a design for an external Helium Bubbling Facility for the Molten Salt Fast Reactor was proposed, on which two-phase simulations using fluid flow and counter-current bubbling were performed. A methodology was developed to calculate extraction efficiencies for small particles from the simulations, based on flotation models studied in literature. Furthermore, experiments were thought out and partly performed to study the behaviour of a porous plate sparger in a bubble column and to validate the flotation models.

The simulations showed that an external helium bubbling facility, using counter current bubbling, has the potential to be an effective means of metallic fission product removal. Even though the efficiencies for sub-micron particles are still low, using co-current bubbling as is currently considered in the MSFR would make them even lower due to the Airation Length being much smaller as a result of the bubbles going with the salt flow. Using an external facility instead, gives the opportunity of choosing the optimal flow and bubbling conditions for effective removal of metallic particles from the fuel salt. In the currently used MSFR designs, not only is there much less freedom with regard to choosing flow and bubbling conditions, it is also not worked out how exactly the metallic fission products are removed after being bubbled to the surface (where the *gas* is removed to the off-gas system). In an External Helium Bubbling Facility, such a system can easily be included without the need to reconsider other design aspects of the reactor.

With respect to the experiments on the flotation models, even though they could largely not be carried out, significant progress was made in the development of an experiment that can be carried out in the future to validate flotation models using Laser Induced Fluorescence. Since these experiments have not been carried out in this research, there is no data to present to NRG to validate their code with at this moment. However, using the experiment described in this research, this data can be generated in the future.

6.3. Recommendations
6.3.1. Simulations
With respect to the numerical part of this thesis, there is a number of things to consider in follow-up research. Firstly, it should be **expanded to 3D** to make more quantitatively appropriate predictions of the efficiency of the facility and the uncertainties and/or errors. Also, extraction efficiencies for larger particles could be calculated for instance **using a three-phase solver**. Furthermore, once this has been achieved, **flotation models could be incorporated in the code** instead of doing the calculations on flotation in the post-processing of the data. With these elements included, **optimization studies** can be performed to find the design aspects and flow conditions that give the greatest efficiency. Lastly, **a collecting system for the froth layer** (or the overflow of salt containing large amounts of fission products) should be designed and eventually incorporated.

6.3.2. Experiments
As for the experimental part, in above section it was concluded that the found bubble Sauter diameter did not correspond to the value expected from literature. Therefore, with the advantages of small bubbles in flotation in mind, the **relation between sparger layout and flow parameters should be investigated for small pore sizes and low gas flow rates**.

Furthermore, since the aim is to utilise fuel salt flow, it should be considered if a different setup would be preferable as the currently used one does not **allow counter-current bubbling**. Another reason is the trouble arising from the use of the current sparger, which was rather cumbersome in use as described before. I would propose a **new sparger layout** as shown here:
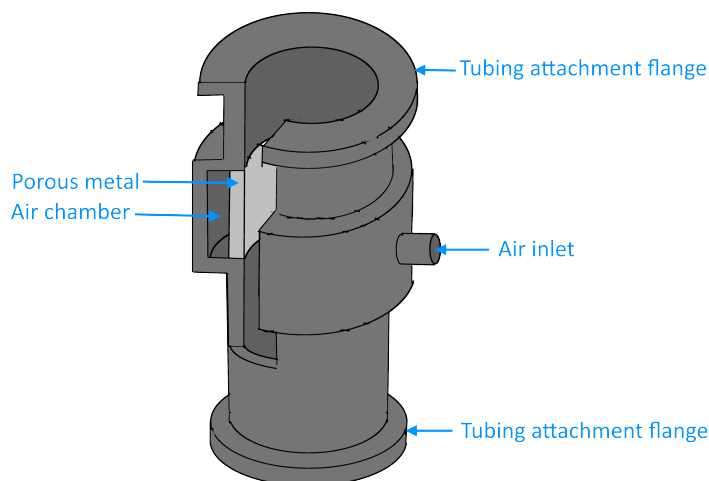

Figure 6.2: Proposal for the sparger layout for future experiments on flotation and/or bubble behaviour. The porous metal is welded in place.

With a sparger setup like this, the problem of the pourous plate sparger being a separate piece that has to be clamped and sealed will no longer be an issue. Also, it would make it possible to **examine counter-current bubbling**, which is impossible when a Venturi-tube is used.

As for the flotation column itself, if measurements relying on optics are going to be used (such as LIF), it might be an idea to use a **transparent (perspex) column that is circular on the inside but square on the outside**, to minimise light signal distortion due to shape. Since water and perspex have a similar refraction index, it is mostly the perspex-air interface that causes this distortion. Building a transparent, square container filled with water around a circular flotation column might therefore give the same result (and save a considerable amount of money).

Lastly, the **effect of adding flocculants** could be studied. Flocculants help apolar particles in a polar liquid (or vice-versa) cluster together, increasing their effective size and therefore possibly increase their flotation probability.

6.3.3. Increasing the efficiency of an External Helium Bubbling Facility in the MSFR

As mentioned, the Helium Bubbling Facility presented in this thesis has relatively low extraction yields. There are a number of ways in which this efficiency might be increased:

- **Adding a flocculant**
  As mentioned above, flocculants help particles stick together. Adding a flocculant to the fuel salt when it enters the Helium Bubbling Facility might therefore help increase the efficiency with which it removes metallic particles. However, the flocculant itself must not have a negative influence on the further reactor operation, or should be removed at the exit of the Helium Bubbling Facility.

- **Lower the Salt Flow Rate**
  Lowering the salt flow rate will lead to lower salt velocities inside the facility, as well as making the average duration of stay of a volume of salt in the facility larger. The first effect means that the Airation Length will be increased, causing a higher extraction yield *and* allowing for smaller bubble sizes (which

also give greater efficiencies). The second effect means that the effective bubbling time for a volume in salt increases, which too will lead to higher extraction yields.

- **Using smaller bubbles**
  As mentioned in previous point, smaller bubbles yield higher extraction efficiencies. If the bubbles are too small however, they will be taken by the salt flow and not be effective for flotation purposes. Therefore, using smaller bubbles should be done in combination with a corresponding lowering of the salt flow rates.

6.3.4. Molybdenum as medical isotope

A final word about the extraction of Molybdenum. Since Molybdenum-99 is very important in Nuclear Medicine, being able to extract it from a Molten Salt Reactor as a byproduct of energy production is a great opportunity to obtain more medical isotopes using as little Nuclear Facilities as possible. Furthermore, a reactor that produces both energy and medical isotopes might be much less 'scary' in the eyes of the public, causing a much greater support base. Therefore, trying to remove Molybdenum from the fuel salt and after that actually isolate it, would be a great step in the direction of giving Nuclear Energy and Reactors as a whole a more positive image in the public opinion.

Bibliography

[1] Hannah Ritchie. Energy. *Our World in Data*, 2014. https://ourworldindata.org/energy.

[2] John J. Conti et al. *Annual Energy Outlook 2016*. U.S. Energy Information Administration, 2016. DOE/EIA-0383(2016).

[3] Peter Bronski. You down with lcoe? maybe you, but not me. Rocky Mountain Institute, `https://web.archive.org/web/20161028152421/http://blog.rmi.org/blog_2014_05_29_you_down_with_lcoe`, 2014.

[4] S. Byrom. Lcoe is dead! EnergyCentral (part of EnergyBiz Network), `https://energycentral.com/c/pip/lcoe-dead`, 2019.

[5] S. Shah and M. Bazilian. Lcoe and its limitations. Energy for Growth Hub, `https://www.energyforgrowth.org/memo/lcoe-and-its-limitations/`, 2020.

[6] H. Axelrod and D. Shawhan. Levelized cost of energy - making economic sense of energy options. Georgia Institute of Technology, `https://web.archive.org/web/20150912142057/http://secleanenergy.gatech.edu/wp-content/uploads/2013/09/20130925_axelrod.pdf`, 2013.

[7] World Nuclear Association. Radioactive waste management. World Nuclear Association, `https://www.world-nuclear.org/information-library/nuclear-fuel-cycle/nuclear-wastes/radioactive-waste-management.aspx`, 2020.

[8] Kazuo Furukawa, Eduardo Greaves, L. Erbay, Miloslav Hron, and Yoshio Kato. *New Sustainable Secure Nuclear Industry Based on Thorium Molten-Salt Nuclear Energy Synergetics (THORIMS-NES)*. IntechOpen, 09 2011. ISBN 978-953-307-474-0. doi: 10.5772/19198.

[9] NOS. Meerderheid tweede kamer voor kernenergie, maar of het ervan komt? NOS, `https://nos.nl/artikel/2258185-meerderheid-tweede-kamer-voor-kernenergie-maar-of-het-ervan-komt.html`, 2018.

[10] World Nuclear Association. Nuclear fuel cycle overview. World Nuclear Association, `https://www.world-nuclear.org/information-library/nuclear-fuel-cycle/conversion-enrichment-and-fabrication/uranium-enrichment.aspx`, 2020.

[11] Atomic Archive. Nuclear fission: Basics. AtomicArchive.com, `http://www.atomicarchive.com/Fission/Fission1.shtml`, 2020.

[12] World Nuclear Association. Nuclear fuel cycle overview. World Nuclear Association, `https://www.world-nuclear.org/information-library/nuclear-fuel-cycle/introduction/nuclear-fuel-cycle-overview.aspx`, 2020.

[13] Robert Hargraves and Ralph Moir. Liquid fluoride thorium reactors. *American Scientist*, 98:304–313, 2010. URL `https://web.archive.org/web/20131208020100/http://www.energyfromthorium.com/pdf/AmSci_LFTR.pdf`.

[14] Giorgio Locatelli, Mauro Mancini, and Nicola Todeschini. Generation iv nuclear reactors: Current status and future prospects. *Energy Policy*, 61:1503 – 1520, 2013. ISSN 0301-4215. doi: https://doi.org/10.1016/j.enpol.2013.06.101. URL `http://www.sciencedirect.com/science/article/pii/S0301421513006083`.

[15] John E. Kelly. Generation iv international forum: A decade of progress through international cooperation. *Progress in Nuclear Energy*, 77:240 – 246, 2014. ISSN 0149-1970. doi: https://doi.org/10.1016/j.pnucene.2014.02.010. URL `http://www.sciencedirect.com/science/article/pii/S0149197014000419`.

[16] M. Allibert, M. Aufiero, M. Brovchenko, S. Delpech, V. Ghetta, D. Heuer, A. Laureau, and E. Merle-Lucotte. 7 - molten salt fast reactors. In Igor L. Pioro, editor, *Handbook of Generation IV Nuclear Reactors*, Woodhead Publishing Series in Energy, pages 157 – 188. Woodhead Publishing, 2016. ISBN 978-0-08-100149-3. doi: https://doi.org/10.1016/B978-0-08-100149-3.00007-0. URL http://www.sciencedirect.com/science/article/pii/B9780081001493000070.

[17] R.H. Guymon. Msre systems and components performance. Report ORNL-TM-3039, Oak Ridge National Laboratory, 1973. URL https://www.osti.gov/biblio/4462915-msre-systems-components-performance.

[18] Elisa Capelli. Molten salt chemistry - final project report. Technical report, Delft University of Technology, 2019.

[19] Jan Leen Kloosterman. Samofar (safety assessment of the molten salt fast reactor) jan leen kloosterman @thec2018. YouTube presentation, https://www.youtube.com/watch?v=5WXALiUE0S0, 2018.

[20] W.L. Carter. Decay heat generation by fission products and 233pa in a single-region molten salt reactor. Report CF-68-3-38, Oak Ridge National Laboratory, 1968. URL https://www.osti.gov/servlets/purl/1524590.

[21] R.J. Kedl. The migration of a class of fission products (noble metals) in the molten-salt reactor experiment. Report ORNL-TM-3884, Oak Ridge National Laboratory, 1972.

[22] J.A. Lane and U.S. Atomic Energy Commission. *Fluid Fuel Reactors*. Addison-Wesley books in nuclear science and metallurgy. Addison-Wesley Publishing Company, 1958. URL https://books.google.nl/books?id=9L4jAAAAMAAJ.

[23] J.W. Koger. Evaluation of hastelloy-n alloys after nine years exposure to both a molten fluoride salt and air at temperatures from 700 to 560°c. Report ORNL-TM-4189, Oak Ridge National Laboratory, 1972.

[24] J. Kopecky. Atlas of neutron capture cross sections. Report INDC(NDS)-362, International Atomic Energy Agency, 1997.

[25] E.L. Compere, E.G. Bohimann, S.S. Kirslis, F.F. Blankenship, and W.R. Grimes. Fission product behaviour in the molten salt reactor experiment. Report ORNL-TM-4189, Oak Ridge National Laboratory, 1975.

[26] F.N. Peebles. Removal of xenon-135 from circulating fuel salt of the msbr by mass transfer to helium bubbles. Report ORNL-TM-2245, Oak Ridge National Laboratory, 1968.

[27] C.H. Gabbard. Development of a venturi type bubble generator for use in the molten-salt reactor xenon removal system. Report ORNL-TM-4122, Oak Ridge National Laboratory, 1972.

[28] N. A. Kazakis, A. A. Mouza, and S. V. Paras. Experimental study of bubble formation at metal porous spargers: Effect of liquid properties and sparger characteristics on the initial bubble size distribution. *Chemical Engineering Journal*, 137(2):265–281, 2008. doi: doi:10.1016/j.cej.2007.04.040. URL https://www.sciencedirect.com/science/article/abs/pii/S1385894707003117.

[29] Wouter Koen Harteveld. *BUBBLE COLUMNS: Stuctures or Stabibity?* PhD thesis, Delft University of Technology, 2005.

[30] Elisa Capelli. Notes on flotation. Report, Delft University of Technology, 12 2016.

[31] R. Krishna and J.M. van Baten. Mass transfer in bubble columns. *Catalysis Today*, 79-80:67–75, 2003. URL https://doi.org/10.1016/S0920-5861(03)00046-4.

[32] J.R. Engel and R.C. Steffy. Xenon behaviour in the molten salt reactor experiment. Report ORNL-TM-3464, Oak Ridge National Laboratory, 1971. URL http://www.thmfgrcs.com/ORNL-TM-3464.pdf.

[33] Ming Zhang. *Removal of nanoparticles by flotation processes.* PhD thesis, INSA de Toulouse, 2015. URL https://tel.archives-ouvertes.fr/tel-01191789/document. HAL-archive id: tel-01191789.

[34] Zongfu Dai, Daniel Fornasiero, and John Ralston. Particle–bubble collision models — a review. *Advances in Colloid and Interface Science*, 85(2):231 – 256, 2000. ISSN 0001-8686. doi: https://doi.org/10.1016/S0001-8686(99)00030-5. URL http://www.sciencedirect.com/science/article/pii/S0001868699000305.

[35] Gan Cheng, Changliang Shi, Xiaokang Yan, Zhijun Zhang, Hongxiang Xu, and Yang Lu. A study of bubble-particle interactions in a column flotation process. *Physicochemical Problems of Mineral Processing*, 53(1):17–33, 2017. ISSN 2084–4735. doi: http://dx.doi.org/10.5277/ppmp170102. URL http://www.minproc.pwr.wroc.pl/journal/pdf/ppmp53-1.17-33.pdf.

[36] S. Kouachi, M. Bouhenguel, A. Amirech, and A. Bouchemma. Yoon–luttrell collision and attachment models analysis in flotation and their application on general flotation kinetic model. *Desalination*, 264 (3):228 – 235, 2010. ISSN 0011-9164. doi: https://doi.org/10.1016/j.desal.2010.06.057. URL http://www.sciencedirect.com/science/article/pii/S0011916410004662. Special Issue to honour the previous editor Miriam Balaban.

[37] Horace Lamb. *Hydrodynamics*, page 599. Cambridge University Press, 6th edition, 1994. ISBN 978-0-521-45868-9. Originally published in 1879, the 6th extended edition appeared first in 1932.

[38] A.V. Nguyen, H.J. Schulze, and J. Ralston. Elementary steps in particle—bubble attachment. *International Journal of Mineral Processing*, 51(1):183 – 195, 1997. ISSN 0301-7516. doi: https://doi.org/10.1016/S0301-7516(97)00030-6. URL http://www.sciencedirect.com/science/article/pii/S0301751697000306. Application of Surface Science to Advancing Flotation Technology.

[39] Eric Cervi, Stefano Lorenzi, Lelio Luzzi, and Antonio Cammi. Multiphysics analysis of the msfr helium bubbling system: A comparison between neutron diffusion, sp3 neutron transport and monte carlo approaches. *Annals of Nuclear Energy*, 132:227 – 235, 2019. ISSN 0306-4549. doi: https://doi.org/10.1016/j.anucene.2019.04.029. URL http://www.sciencedirect.com/science/article/pii/S0306454919302130.

[40] Henrik Rusche. *Computational fluid dynamics of dispersed two-phase flows at high phase fractions*. PhD thesis, University of London, 2002.

[41] François G. Schmitt. About boussinesq's turbulent viscosity hypothesis: historical remarks and a direct evaluation of its validity. *Comptes Rendus Mécanique*, 335(9-10):617–627, 2007. ISSN 1631-0721. doi: https://doi.org/10.1016/j.crme.2007.08.004.

[42] L. Schiller and Z. Naumann. A drag coefficient correlation. *VDI Zeitung*, 77:318–320, 1935.

[43] T. R. Auton. The lift force on a spherical body in a rotational flow. *Journal of Fluid Mechanics*, 183: 199–218, 1987. doi: 10.1017/S002211208700260X.

[44] Shiva P. Pudasaini. A fully analytical model for virtual mass force in mixture flows. *International Journal of Multiphase Flow*, 113:142 – 152, 2019. ISSN 0301-9322. doi: https://doi.org/10.1016/j.ijmultiphaseflow.2019.01.005. URL http://www.sciencedirect.com/science/article/pii/S0301932218307055.

[45] A.D. Gosman, C. Lekakou, S. Politis, R.I.Issa, and M.K. Looney. Multidimensional modeling of turbulent two-phase flows in stirred vessels. *American Institute of Chemical Engineers Journal*, 38:1946–1956, 1992. doi: https://doi.org/10.1002/aic.690381210. URL https://aiche.onlinelibrary.wiley.com/doi/pdfdirect/10.1002/aic.690381210.

[46] Richard W. Fessenden. The viscosity and surface tension of dispersions of sucrose, lactose, skim milk powder, and butterfat. Master's thesis, University of Massachusetts Amherst, 1928.

[47] Sarah M. Monahan and Rodney O. Fox. Validation of two-fluid simulations of a pseudo-two-dimensional bubble column with uniform and nonuniform aeration. *Industrial & Engineering Chemistry Research*, 48(17):8134–8147, 2009. doi: 10.1021/ie801202x. URL https://doi.org/10.1021/ie801202x.

[48] K. Ekambara, Mahesh T. Dhotre, and Jyeshtharaj B. Joshi. Cfd simulations of bubble column reactors: 1d, 2d and 3d approach. *Chemical Engineering Science*, 60(23):6733 – 6746, 2005. ISSN 0009-2509. doi: https://doi.org/10.1016/j.ces.2005.05.047. URL http://www.sciencedirect.com/science/article/pii/S0009250905004963.